SECTION 1

RESEARCH IN PROGRESS

NUCLEAR REACTIONS -- EXPERIMENTAL

TEMPERATURE MEASUREMENTS FOR CENTRAL Au+Au COLLISIONS AT 35 MeV/A

M.J. Huang, H. Xi, W.G. Lynch, M.B. Tsang, J.D. Dinius[a] S.J. Gaff, C.K. Gelbke, T. Glasmacher, G.J. Kunde, L. Martin[b], C.P. Montoya[c], E. Scannapieco[d], P.M. Milazzo, *et.al*
(Miniball/Multics Collaboration)

Theoretically, there is little doubt that infinite nuclear matter undergoes a transition from a liquid to a gaseous phase and supports a mixed phase equilibrium at temperatures up to about 17 MeV[1,2]. Recent experimental evidence for the onset and decline of fragment production with increasing incident energy [3] or deduced excitation energy [4] and the observation of short fragmentation time scales [5,6] reveal many of the necessary conditions for mixed phase equilibrium to be met in present experiments. Despite these promising indications, information about freeze-out temperature and density for bulk disintegrations is necessary to proceed with the accurate extraction of thermodynamic quantities from such collisions. Tests of the validity of the assumption of local equilibrium at freeze-out are necessary to discern non-equilibrium and dynamical effects.

Recent investigations reveal that approximately ten intermediate mass fragment (IMF's: $3 \leq Z \leq 20$) are produced in central Au+Au collisions at E/A=35 MeV [7]. Exceedingly flat charge distributions are observed [7] which calculations predict to be a consequence of the destabilizing Coulomb interaction [8]. Both fragment-fragment correlations and fragment kinetic energy spectra are reasonably well described by the Coulomb driven breakup of single thermalized source [6,7]. These observations have been reasonably well reproduced by Statistical Multifragmentation Model (SMM)[9] calculations wherein the fragments are produced via a bulk multifragmentation at a density of $\rho_0/6 \leq \rho \leq \rho_0/3$ and a temperature of $T \approx 6$ MeV [6]. Tests of the validity of such models, however, are more stringent if the assumed values of the temperature, density or both can be constrained experimentally. In this paper, we provide constraints on the assumed breakup temperature of this Au+Au system via measurements of excited state populations and isotope ratios.

The experiment was performed by bombarding a 5 mg/cm^2 Au target with the 35A MeV Au beam of the National Superconducting Cyclotron Laboratory at Michigan State University. Charged particles were detected in the combined Miniball-Multics array [10,11], which has a geometric acceptance of greater than 87% of 4π.

Light charged particles and IMF's were detected at $3° < \theta_{lab} < 23°$ in the Multics array of 44 gas-Si-CsI telescopes [11]. The position-sensitive Si detector in each Multics telescope provided a two-dimensional angular readout with an angular resolution (0.27° for 5.8 MeV α particles) sufficient for extraction of the excited state populations of emitted fragments. The dynamic range of the electronics for the Multics array was optimized to provide maximum isotopic resolution for $1 \leq Z \leq 6$ and isotopically resolved yields could be determined for emitted $^{1,2,3}H$, $^{3,4,6}He$, $^{6,7,8,9}Li$, $^{7,9,10}Be$, $^{10,11,12,13}B$, and $^{12,13,14}C$ nuclei. Representative identification thresholds of 8.5, 5.5, 4, 8.5, 10.5, 12 and 13.5A MeV were achieved in the Multics array for p, d, t, α, ^6Li, ^9Be, and ^{10}B nuclei, respectively. Energy calibrations accurate to 2% were obtained by irradiating each telescope with ^{228}Th and ^{244}Cm α sources and with low intensity direct beams of α, ^{12}C and ^{16}O particles at 40A MeV, ^9Be at 11.4 and 15.9A MeV, ^{10}Be at 8.1 and 9.3A MeV, ^{10}B at 12.7 and 20.1A MeV, ^{11}B at 10.5 and 12A MeV and ^{12}B particles at 10A MeV. Fragments detected at $v_{lab} > v_{cm}$ in the Multics array were used to extract temperatures.

Light charged particles and fragments with $1 \leq Z \leq 20$ were detected at $23° < \theta_{lab} < 160°$ by 158 fast plastic-CsI phoswich detectors of the MSU Miniball array [10]. Following ref. [7], we assumed that the charged particle multiplicity Nc detected in Miniball array depends monotonically upon the impact parameter

$$\hat{b} = \frac{b}{b_{\max}} = \left[\int_{N_C(b)}^{\infty} dN_C \cdot P(N_C) \right]^{1/2} \tag{1}$$

and assigned a mean "reduced" impact parameter, $\hat{b}$, to each data point using Eq. 1. Here, $P(N_C)$ is the probability distribution for the charged particle multiplicity for $N_C \geq 3$, and b_{max} is the mean impact parameter with $N_C = 3$.

Temperatures determined from the relative yields of different decay channels [12-21] have the advantage of being insensitive to collective motion [22] and Coulomb barrier fluctuations [23]. However, these temperatures do require corrections for secondary decay [13,17-20]. These corrections are more problematic for the relative isotope yields because of their sensitivity to the uncertainties in the isotopic composition of the system at breakup [24-26]. These effects do not strongly influence the excited state populations [26]. To cross check the isotope yield temperatures and to test the attainment of local thermal equilibrium, the relative excited state populations and the isotopic abundances of fragments with $3 \leq Z \leq 6$ were compared. At higher incident energies, isotope ratios have yielded higher temperatures (up to T≈15 MeV) [16] than have the excited state populations [21]; temperatures extracted from the latter have not exceeded T≈6 MeV[14]. A broad impact parameter gate $0 \leq \hat{b} \leq 0.45$ is needed for this comparison because yields of fragments in specific highly excited states are small compared to the yields of stable nuclei. After extracting comparable temperatures with the two methods, the statistically more precise isotope ratio data are extrapolated to $\hat{b} \approx 0$, where previous analyses suggest that fragment emission is dominated by a single source [6,7].

Models which describe the statistical decay of thermalized nuclear systems [12-14] predict that prior to the secondary decay of the excited fragments, the ratio R_{ij} of states i and j of a specific fragment should be given by:

$$R_{ij} = \frac{Y_i}{Y_j} = \frac{(2J_i + 1)}{(2J_j + 1)} e^{-(E_i^* - E_j^*)/T_{app}} \tag{2}$$

where Y_i is the measured yield, E_i^* is the excitation energy and J_i is the spin of the state i. Following techniques described in refs. [13,14], relative populations of specific states of ^{5}Li, ^{4}He, and ^{10}B fragments were measured by detecting the coincident decay products and an "apparent temperature" T_{app} was obtained for each ratio by inverting Eq.2. The leftmost data point in the left panel of Fig. 1 indicates the measured apparent temperature calculated from the yield of the ^{5}Li (E_j^* = 16.66 MeV, $J_j = 3/2^+$) excited state divided by the yield of the ^{5}Li (E_i^* = 0 MeV, $J_i = 3/2^-$) ground state. The middle data point shows the measured apparent temperature calculated from the yield of the ^{4}He (E_j^*= 20.1 MeV, $J_j = 0^+$) excited state divided by the yield of the ^{4}He (E_i^* = 0 MeV, $J_i = 0^+$) ground state. The four excited states of ^{10}B (7.43 MeV, 2^-; 7.467 MeV, 1^+; 7.478 MeV, 2^+; 7.5599 MeV, 0^+) are unresolved. The rightmost data point in the left panel shows the apparent temperature calculated from the sum of the yields of the four ^{10}B excited states divided by the yield of the (4.77 MeV, 3^+) excited state. The error bars of the apparent temperature

reflect both the statistical uncertainty and the uncertainty due to background subtraction. Following

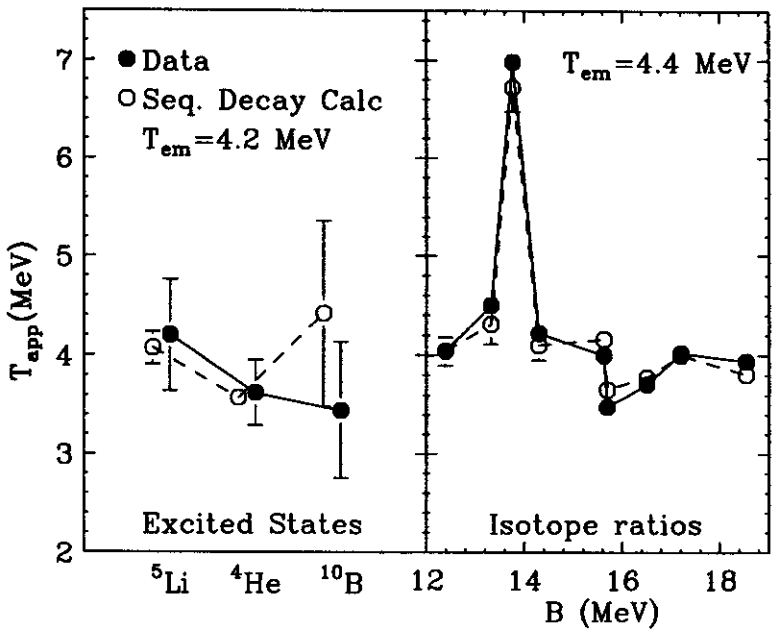

Figure 1: Apparent temperatures obtained from relative populations of excited states for ^{5}Li, ^{4}He and ^{10}B nuclei using Eq.2 (left panel) and from isotope ratios using Eq.3 (right panel). (See also Table I). The closed points are the data and the open points are the predictions of sequential decay calculations.

Albergo *et al.* [15], chemical potential effects were eliminated by constructing double ratios R_{Iso} from the yields of four isotopes to obtain an apparent temperature, T_{app}

$$R_{Iso} = exp(B/T_{app})/a \tag{3}$$

where $R_{Iso} = \{Y(A_1,Z_1)/Y(A_1+1,Z_1)\}/\{Y(A_2,Z_2)/Y(A_2+1,Z_2)\}$; Y(X) is the yield for isotope X; a is a constant determined by spin values and kinematics factors; $B = BE(A_1,Z_1) - BE(A_1+1,Z_1) - BE(A_2,Z_2) + BE(A_2+1,Z_2)$; and $BE(A_i,Z_i)$ is the binding energy of the ith nucleus. We restrict our investigation to thermometers with B values in excess of 10 MeV to reduce fluctuations in the temperature measurement[17]. Table I lists the nine possible double isotope yield ratios with values of a and B computed from the relevant ground state spectroscopic information. Also listed in Table I and shown in the right hand panel in Fig. 1 are the corresponding "apparent temperatures" obtained by inverting Eq.3. The uncertainties reflect the changes in R_{Iso} obtained by choosing different gates on the velocity of the emitted fragments in the center of mass and by considering the sensitivity of the isotopic yields to uncertainties in the precise placement of the isotope gates.

The fluctuations in the "apparent temperatures" from ratio to ratio, shown in Fig. 1, are not a manifestation of non-equilibrium effects but instead are the direct consequences of the secondary decay of highly excited fragments whose decay feeds the measured yields. We have used sequential decay calculations to calculate the modifications to the initial populations of excited states caused by the sequential feeding from heavier particle unstable nuclei. In these calculations, the excited states of primary emitted fragments are populated thermally, and then allowed to decay, using approximations outlined in refs. [13,18,20,26]. Unknown spins or parities of low lying discrete states were assigned

Isotope Ratio	a	B	$T_{app}(\hat{b} < 0.45)$	$T_{app}(\hat{b} \approx 0)$
		(MeV)	(MeV)	(MeV)
$^{13,14}C/^{3,4}He$	0.72	12.39	4.04 ± 0.10	4.04 ± 0.16
$^{6,7}Li/^{3,4}He$	2.18	13.32	4.51 ± 0.02	4.64 ± 0.05
$^{9,10}Be/^{3,4}He$	0.38	13.76	7.00 ± 0.24	7.8 ± 10.9
$^{2,3}H/^{3,4}He$	1.59	14.29	4.21 ± 0.01	4.42 ± 0.04
$^{12,13}C/^{3,4}He$	2.94	15.62	4.00 ± 0.05	4.15 ± 0.08
$^{12,13}B/^{3,4}He$	1.95	15.69	3.48 ± 0.02	3.47 ± 0.03
$^{8,9}Li/^{3,4}He$	1.24	16.51	3.71 ± 0.02	3.79 ± 0.07
$^{11,12}B/^{3,4}He$	1.11	17.20	4.02 ± 0.03	4.20 ± 0.08
$^{7,8}Li/^{3,4}He$	1.98	18.54	3.94 ± 0.01	4.04 ± 0.03

Table 1: List of isotope ratio thermometers with $B > 10MeV$ and the corresponding measured apparent temperatures. The uncertainties in T_{app} are larger for $\hat{b} \approx 0$ than for the broad impact parameter gate $0 \leq \hat{b} \leq 0.45$ reflecting uncertainties in the extrapolation to $\hat{b} \approx 0$.

randomly and the calculations were repeated to assess the sensitivities of the population probabilities and isotope ratios to these spectroscopic uncertainties. This unknown spectroscopic information contributes a 5% uncertainty to the calculated ratios. An additional 8% uncertainty stemming from the unknown isotopic composition of the emitting system at freeze-out was assessed by varying the assumed N/Z ratio of the decaying system. These are the major uncertainties that our investigation have shown to influence the secondary decay corrections [20,26].

These calculations were performed for initial temperatures ranging from 2 MeV to 6 MeV and the agreement between theory and experiment was assessed by calculating corresponding values for the reduced χ^2 using the expression,

$$\chi^2_\nu(T_{em}) = \frac{1}{\nu}\sum_{i=1}^{\nu}\frac{[R_{expt,i} - R_{calc,i}(T_{em})]^2}{\sigma^2_{expt,i} + \sigma^2_{calc,i}} \tag{4}$$

independently for the isotope ratios and for the excited state populations. Here the $\sigma_{expt,i}$ and $\sigma_{calc,i}$ are the experimental and theoretical uncertainties and the summation runs over the relevant excited state populations or isotope ratios. The solid and dashed lines in the upper panel of Fig. 2 show the χ^2_ν values for isotope ratios and excited state populations for $0 \leq \hat{b} \leq 0.45$. The calculated χ^2_ν curves are asymmetric reflecting a gradual reduction of the sensitivity of $R_{calc}(T_{em})$ to T_{em} with increasing temperature [26]. From the shape and minima of the calculated curves, best fit values of 4.4 ± 0.2 MeV and 4.2 ± 0.6 MeV [27] are determined for the isotope ratios and excited state populations, respectively; this indicates that the two thermometers provide equivalent information at E/A=35 MeV, in contrast to the results reported [16,21] at significantly higher energies. The best fit values for the calculated "apparent temperatures", shown as the open points in Fig. 1, well reproduce the experimental data.

This good agreement implies that the ensemble of emitted particles are well described by the assumption of local thermal equilibrium provided that T_{em} is not strongly impact parameter dependent. To investigate this impact parameter dependence using the higher statistical precision of the isotope ratio data, we analyzed the apparent isotope temperatures as a function of $\hat{b}$ for gates on $\hat{b}$ of $\hat{b} \approx$

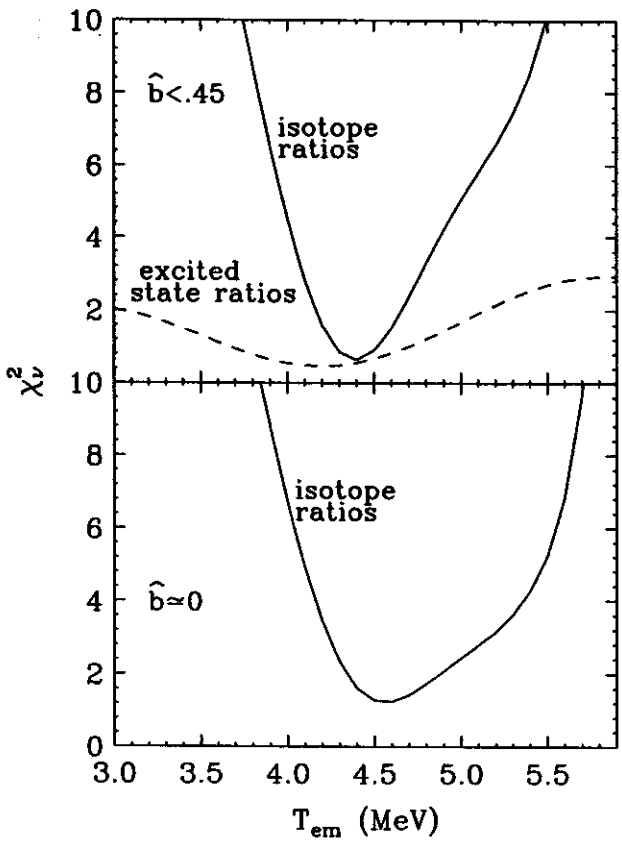

Figure 2: Results of the least squares analysis (Eq.4) for the relative populations of excited states of ^{5}Li, ^{4}He and ^{10}B nuclei, (dashed line) and for the nine isotope double yield ratios (solid lines) at $\hat{b} < 0.45$ (top panel) and $\hat{b} \approx 0$ (bottom panel).

$0.08, 0.16, 0.25, 0.35, 0.45 \pm 0.05$ and observed an approximately linear dependence of R_{Iso} upon $\hat{b}$ and obtained the values listed in Table I for $\hat{b} \approx 0$ via straight line extrapolation.

The minimum in the corresponding χ^2_ν function for $\hat{b} \approx 0$, shown in the lower panel of Fig. 2, provides a temperature of $T_{em} = 4.6 \pm 0.4$ MeV [27], which is similar to the result at $0 \leq \hat{b} \leq 0.45$. This indicates a weak impact parameter dependence of T_{em} consistent with, but not requiring, dominant emission by a central participant source formed by the overlap of projectile and target nuclei. Significant differences between an ideal measurement at zero impact parameter and the present data at $\hat{b} \approx 0$ are rendered unlikely by this weak impact parameter dependence even though impact parameter scales become imprecise at small impact parameters. Finally, the extracted value $T_{em} = 4.6 \pm 0.4\ MeV$ at $\hat{b} \approx 0$ is comparable to values obtained for other multifragmenting systems[18,19].

In summary, we have measured breakup temperatures for Au+Au reactions at 35A MeV. Temperatures extracted from isotope ratios and excited state populations are virtually the same for a broad impact parameter gate of $0 \leq \hat{b} \leq 0.45$ consistent with the attainment of local thermal equilibrium. Extrapolating these measurements to $\hat{b} \approx 0$ yields a breakup temperature of $4.6 \pm 0.4\ MeV$, somewhat lower than that assumed by SMM calculations which reproduce well the other experimental observables for this reaction.

a. Present address: Baker Hill, 655 W. Carmel Dr. Suite 100, Carmel IN 46032, USA.

b. Present address: Laboratoire de Physique Subatomique, 44070 Nantes Cedes 03 France.
c. Present address: Merrill Lynch, World Financial Center, New York, NY 10281, USA.
d. Present address: MIT, Cambridge, MA, USA.

References

1. W.G. Lynch, Ann. Rev. Nucl. Part. Sci. 37, 493, (1987) and references therein.
2. G. Sauer, H. Chandra, U. Mosel, Nucl. Phys. A264, 221 (1976); H.R. Jaqaman, A.Z. Mekjian, L. Zamick, Phys. Rev. C27, 2782 (1983), C29, 2067 (1984); M.W. Curtin, H. Toki, D.K. Scott, Phys. Lett. B123, 289 (1983).
3. M.B. Tsang et al, Phys. Rev. Lett. 71, 1502 (1993); G.F. Peaslee et al., Phys. Rev. C49, R2271 (1994).
4. C.A. Ogilvie et al., Phys. Rev. Lett 67, 1214 (1991).
5. Roy A. Lacey et al., Phys. Rev. Lett. 70, 1224 (1993); E. Cornell et al., Phys. Rev. Lett. 75, 1475 (1995); O. Lopez et al., Phys. Lett. B 315, 34 (1993).
6. M. D'Agostino et al., Phys. Lett. B 368, 259 (1996); M. D'Agostino et al., Phys. Lett. B 371, 175 (1996)
7. M. D'Agostino et al., Phys. Rev. Lett. 75, 4373 (1995).
8. J. Pan and S. DasGupta, Phys. Rev. C51, 1384 (1995).
9. J.P. Bondorf et al., Phys. Rep. 257, (1995) 133; A.S. Botvina et al., Nucl. Phys. A475, 663 (1987)
10. R.T. De Souza, Nucl. Inst. and Meth. Phys. Res. A295, 109 (1990).
11. P.F. Mastinu et al., Nucl. Instr. and Meth. Phys. Res. A338, 419 (1994) and references therein.
12. D.J. Morrissey, W. Benenson, and W.A. Friedman, Ann. Rev. Nucl. Part. Sci. 44, 27 (1994) and references therein.
13. F. Zhu et al., Phys. Rev. C52, 784 (1995); T.K. Nayak et al., Phys. Rev. C45, 132 (1992); J. Pochodzalla et al. Phys. Rev. C35, 1695 (1987); J.B. Natowitz et al., Phys. Rev. C48, 2074 (1993).
14. C. Schwarz et al., Phys. Rev. C48, 676 (1993) and references therein.
15. S. Albergo et al., Nuovo Cimento 89, 1 (1985).
16. J. Pochodzalla et al., Phys. Rev. Lett. 75, 1040 (1995).
17. M.B. Tsang et al., NSCL preprint 1035 (1996).
18. M.B. Tsang et al., Phys. Rev. C53, R1057 (1996).
19. A. Kolomeits et al., Phys. Rev. C54, R472 (1996).
20. H. Xi, W.G. Lynch, M.B. Tsang, W.A. Friedman, Phys. Rev. C54, R2163 (1996).
21. V. Serfling, Ph. D. Thesis, University of Frankfurt, (1996); J. Pochodzalla, Proceedings of First Catania Relativistic Ion Studies, Acicastello, Italy, May 27-31, (1996).
22. W.C. Hsi et al., Phys. Rev. Lett. 73, 3367 (1994); M.B. Tsang et al., Phys. Rev. Lett. 52, 1967 (1984).
23. L.G. Moretto, Nucl. Phys. A247, 211 (1975).
24. Horst Müller, and Brian D. Serot, Phys. Rev. C52, 2072 (1995).
25. G.J. Kunde et al., Phys. Rev. Lett. 77, 2897 (1996).
26. H. Xi et al., to be published.
27. These errors include contributions from the experimental and theoretical uncertainties, $\sigma_{expt,i}$ and $\sigma_{calc,i}$ respectively.

NUCLEAR THERMOMETERS FROM ISOTOPE YIELD RATIOS

M. B. Tsang, W. G. Lynch, H. Xi, and W. A. Friedman[a]

If chemical and thermal equilibrium are achieved, one may obtain temperature information from a double isotope ratio defined by[1]

$$T_o = \frac{B}{\ln(a \cdot R_o)} \tag{1}$$

where R_o is the ground state fragment yield ratio,

$$R = \frac{Y(A_i, Z_i)/Y(A_i + \Delta A, Z_i + \Delta Z)}{Y(A_j, Z_j)/Y(A_j + \Delta A, Z_j + \Delta Z)} \tag{2}$$

B is a binding energy parameter and a is the statistical factor that depends on statistical weights of the ground state nuclear spins. In particular,

$$B = BE(A_i, Z_i) - BE(A_i + \Delta A, Z_i + \Delta Z) - BE(A_j, Z_j) + BE(A_j + \Delta A, Z_j + \Delta Z), \tag{3}$$

$$a = \frac{(2S(A_j, Z_j) + 1)/(2S(A_j, +\Delta A, Z_j + \Delta Z) + 1)}{(2S(A_i, Z_i) + 1)/(2S(A_i, +\Delta A, Z_i + \Delta Z) + 1)} \left[\frac{A_j/(A_j + \Delta A_j)}{A_i/(A_i + \Delta A_i)}\right]^{1.5} \tag{4}$$

Here, $Y(A_i,Z_i)$, $BE(A_i, Z_i)$ and $S(A_i, Z_i)$ are the yield, known binding energy and ground state spin of a fragment with mass A_i and charge Z_i.

Experimentally one cannot measure T_o directly. Instead, one can only construct the "apparent" temperatures

$$T_{app} = \frac{B}{\ln(a \cdot R_{app})} \tag{5}$$

from experimentally measured fragment yield ratios R_{app} that are altered from the equilibrium values by the effects of sequential decays and other processes neglected by the simple theoretical model of Eq. 1.

The effects of sequential decay and the accuracy of Eq. 1 can be addressed by examining the consistency of a large number of such double ratio "thermometers". Until now, tests have been performed using a few ($\leq$10) thermometers constructed from the yields of H, He, Li, Be, B and C[1 – 7] nuclei. To construct a more significant test, we utilized the detailed inclusive isotope data obtained at Fermilab from proton collisions on Xe at E_p = 80 to 350 GeV/c by the Purdue group [8]. The set of data consists of cross section measurements for 80 species ranging from Lithium to Silicon isotopes. Using Eq. 5, we have constructed 1326 thermometers assuming $\Delta Z = 0$ and $\Delta A = 1$. The left panel of Figure 1 shows the distributions of apparent temperatures from these thermometers as a function of the binding energy difference B. To quantify the feeding effects, we define a correction factor, κ, for each ratio by the relationship $R_{app} = \kappa R_o$ where R_{app} is the measured and R_o, the equilibrium values of the double isotope ratios. It follows from the definition of Eq. 5 that

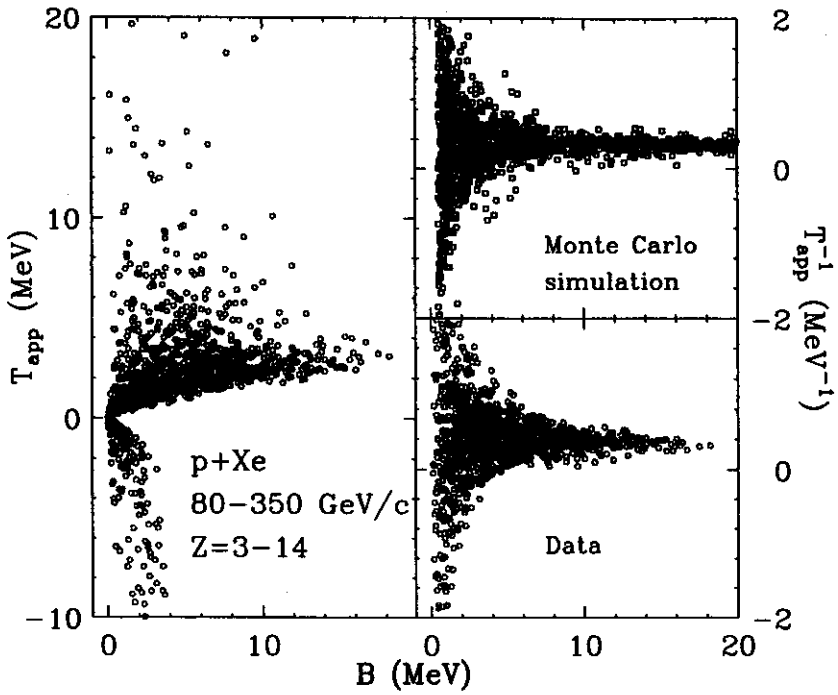

Figure 1: Apparent temperature as a function of binding energy parameter for $p + Xe$ system (left panel). The lower right panel shows the same data plotted as inverse apparent temperatures. The upper right panel shows the results of the Monte Carlo simulations discussed in the text.

$$\frac{1}{T_{app}} = \frac{1}{T_o} + \frac{\ln k}{B} \tag{6}$$

The general features of the fluctuations in $\frac{1}{T_{app}}$ can be reproduced as shown in the top right panel of Fig. 1 by performing Monte Carlo simulations assuming all fragment yields in Eq. 1 fluctuate about their equilibrium values according to a single Gaussian distribution whose variance is 40% of the mean[2]. If such fluctuations reflect structure effects in the sequential decay, they should also appear for other reactions. We have analyzed additional isotope yield data measured for $^{14}N + Ag$ collisions at $E/A = 35$ MeV[9] and $^{32}S + Ag$ collisions at $E/A = 22$ MeV[10] where emission temperatures of 4.0 ± 0.5 MeV and 3.5 ± 0.5 MeV were extracted, respectively, from the relative populations of excited states. For the latter two systems, however, the range of isotopes measured ($3 \leq Z \leq 8$) is more limited than for the $p + Xe$ reaction. Therefore, only 18 isotope ratios ($\Delta Z = 0$, $\Delta A = 1$) with $B > 10$ MeV, common to all three systems are studied. The ratios used in constructing the thermometers and their associated B values are listed in Table I. The apparent temperatures are plotted as open circles in Fig. 2. Thermometers that yield high (low) values for the apparent temperatures for the $p + Xe$ reaction generally yield the same high (low) values for the other two reactions.

To verify that such fluctuations can arise from sequential feedings, the predictions of the published sequential decay calculations which include γ-decays, particle unstable states and unbound states in the continuum for the $N + Ag$ system with an initial temperature of 4 MeV [9] are shown as open squares in the upper right panel of Fig. 2. These predicted values for T_{app} qualitatively follow the experimental

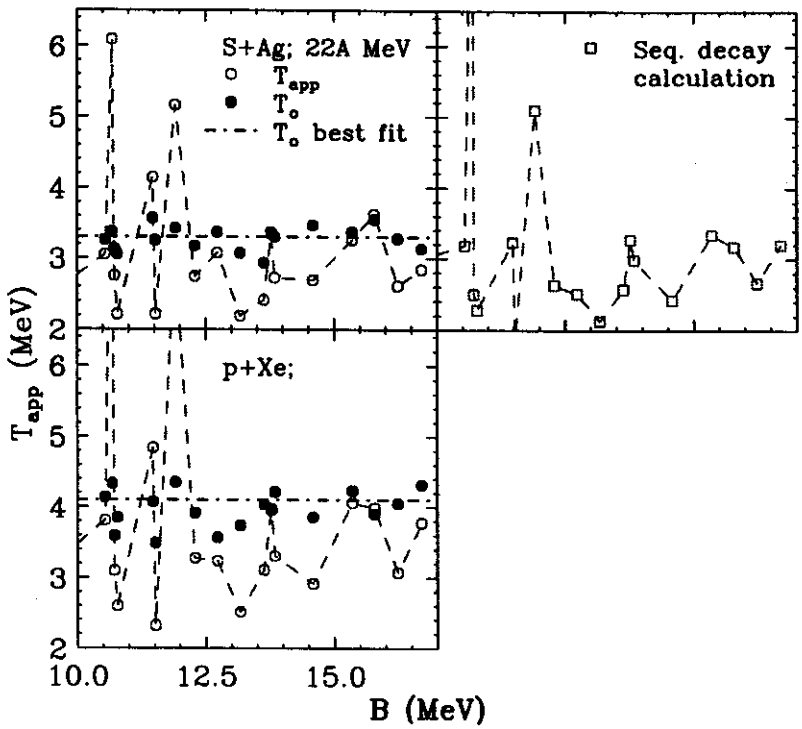

Figure 2: Apparent temperatures as a function of $B > 10$ MeV for $p + Xe$, $S + Ag$ and $N + Ag$ systems. The open circles are raw data and closed circles correspond to corrected temperature calculated according to Eq. 6 (see text for details) . Dashed lines are drawn to guide the eye. The upper right panel shows the apparent temperatures determined from the sequential decay calculations of Ref. [9].

trends seen for the three systems in Fig. 2, indicating that much of the structure information that leads to enhanced emission for one isotope relative to another is already contained in the calculations. Due in part to the inability for the present sequential decay calculations to reproduce isotope distributions for proton rich isotopes such as ^{11}C and ^{15}O accurately, the calculations are not in perfect agreement with the measured apparent temperatures for $N + Ag$ system[9] even for those thermometers with large B. These discrepancies are under current investigation [11].

In the absence of a secondary decay calculation that reproduces the distributions of proton rich nuclei such as ^{11}C and ^{15}O accurately, we adopt a best fit procedure by fitting the data points shown in Fig. 2. Of the 18 isotope ratios shown in Table I, four of them, $^{12,13}C/^{15,16}O$, $^{12,13}B/^{15,16}O$, $^{16,17}O/^{11,12}C$ and $^{11,12}B/^{11,12}C$ are interrelated with the remaining ratios. We used 17 parameters, to fit 14x3=42 data points assuming: 1.) the $ln\kappa/B$ factor for each thermometer is independent of reactions studied, 2.) only one break up temperature (T_o) is obtained for each reaction 3.) The values of T_o should be consistent with the temperatures measured by the relative populations of the excited states. The resulting best fit values are: $T_o = 4.1 \pm 0.4$ MeV and 3.3 ± 0.3 MeV for the $N + Ag$ system and the $S + Ag$ system, respectively. The extracted T_o value for the $p + Xe$ reaction at 80-350 GeV/c is nearly identical to the $N + Ag$ reaction at 35A MeV incident energy. The mean values of $ln\kappa/B$ obtained from the three reactions are listed in Table I.

As an internal consistency test, we can use the values for $< ln\kappa/B >$ listed in Table 1 and Eq. 6 to extract temperatures for each thermometer in each reaction. The resulting temperatures, shown as solid points in Fig 2, follow the T_o values (dot-dashed line) very closely, indicating that the remaining fluctuations are much less than observed for the raw data. These remaining fluctuations may reflect non-equilibrium

Table 1: List of thermometers with $B > 10$ MeV and the extracted correction factors $< \ln(\kappa)/B >$.

Isotope Ratio	B (MeV)	a	$< ln\kappa/B >$ (MeV^{-1})	Isotope Ratio	B (MeV)	a	$< ln\kappa/B >$ (MeV^{-1})
$^{13,14}C/^{11,12}C$	10.54	1.96	0.021	$^{15,16}N/^{15,16}O$	13.17	5.00	0.131
$^{17,18}O/^{11,12}C$	10.68	0.64	-0.132	$^{7,8}Li/^{15,16}O$	13.63	2.77	0.074
$^{12,13}C/^{15,16}O$	10.72	4.09	0.044	$^{12,13}C/^{11,12}C$	13.77	7.92	0.0015
$^{12,13}B/^{15,16}O$	10.78	2.73	0.125	$^{12,13}B/^{11,12}C$	13.84	5.28	0.065
$^{6,7}Li/^{11,12}C$	11.47	5.90	-0.039	$^{16,17}O/^{11,12}C$	14.58	23.07	0.083
$^{16,17}O/^{15,16}O$	11.52	11.93	0.145	$^{11,12}B/^{11,12}C$	15.35	3.00	0.010
$^{9,10}Be/^{11,12}C$	11.91	1.03	-0.098	$^{8,9}Li/^{11,12}C$	15.78	3.35	-0.006
$^{11,12}B/^{15,16}O$	12.29	1.55	0.049	$^{15,16}N/^{11,12}C$	16.23	9.67	0.078
$^{8,9}Li/^{15,16}O$	12.73	1.73	0.028	$^{7,8}Li/^{11,12}C$	16.69	5.36	0.033

effects in the breakup process [9] or the possibility that these inclusive data may have contributions from several sources with different Z/A[11].

a. Department of Physics of Wisconsin, Madison,Wisconsin 53706

References

1. S. Albergo et al., Nuovo Cimento 89, 1 (1985).
2. J. Pochodzalla et al., Phys. Rev. Lett. 75, 1040 (1995).
3. A. Kolomeits et al., Phys. Rev. C54, R472 (1996).
4. M. J. Huang et al., Phys. Rev. Lett., 78, 1648 (1997).
5. H. Xi et al., MSU preprint, MSUCL-1055, (1997).
6. R. Wada et al., Phys. Rev. C55, 227 (1997).
7. Y. Ma et al., Phys. Lett. B41 390(1997).
8. A. S. Hirsch et. al., Phys. Rev. C29, 508 (1984).
9. T. K. Nayak et al., Phys. Rev. C45, 132 (1992).
10. H. M. Xu et. al., Phys. Rev. C40, 186 (1989).
11. H. Xi et al, to be published

SECONDARY DECAYS AND THE HELIUM LITHIUM ISOTOPE THERMOMETER

H. Xi, W.G. Lynch, M.B. Tsang, and W.A. Friedman[a]

Recently analyses of isotopic yields for multifragment decays of $Au + Au$ collisions at $E/A = 600$ MeV yield temperatures that remain relatively constant as a function of deduced excitation energy for 2.5 MeV$\leq E^*/A \leq$ 10 MeV but increase rapidly at $E^*/A \geq 10$ MeV [1]. The evidence of the rapid increase in the temperature at $E^*/A \geq 10$ MeV reported in ref. [1] relies primarily upon the extraction of temperature from the expression [1, 8]

$$T_{HeLi} = C\frac{13.32}{\ln(2.18R_{HeLi})} \tag{1}$$

where $R_{HeLi} = \{Y(^6Li)/Y(^7Li)\}/\{Y(^3He)/Y(^4He)\}$, $Y(X)$ is the yield for isotope X and C is a constant which assumes the value, $C = 1$, in the ideal case that $Y(X)$ are the ground state yields consistent with global thermal and chemical equilibrium. However, the observed populations of isotopes are influenced strongly by the sequential decay of heavier particle unstable nuclei which occurs after these nuclei leave the disintegrating system. In reference [1], C was set to 1.2 in an attempt to correct for such effects.

To address questions relating to the emission temperature, we allow the emission of nuclei with $1 \leq Z \leq 20$ in their ground states or in any of their excited states. The spectrum of allowed excited states includes both the known and tabulated [15] excited states as well as an empirically based extrapolation of the level density into the continuum as described in ref. [12,14]. We approximate the emission by two stages: 1) a first stage where these states are initially populated when the fragments are emitted from the system, and 2) a second stage during which the excited fragments decay according to standard statistical theory.

We assume that the first stage of emission can be described by statistical decay mechanisms; possible candidates range from the evaporation from a heavy residue to the complete vaporization of the system. For simplicity, we approximate the initial population of an excited state of an emitted nucleus with excitation energy E_i^*, spin J_i , neutron number N_i and charge number Z_i with the expression

$$P_i(N_i\ ,\ Z_i\ ,\ E_i^*, \mu_p, \mu_n, T_{em})_\alpha$$
$$(2J_i+1)\cdot(N_i+Z_i)^{1.5}\exp(-\tfrac{V_i}{T_{em}}+\tfrac{Q_i}{T_{em}})\exp(-\tfrac{E_i^*}{T_{em}})\exp(-\tfrac{Z_i\mu_p+N_i\mu_n}{T_{em}})\exp(-t_b/t_i), \tag{2}$$

where V_i is the Coulomb barrier, $-Q_i$ is the separation energy for emission of this nucleus from a residue of mass number A_o and charge number Z_o, T_{em} is the emission temperature and $\exp(-t_b/t_i)$ is a factor which suppresses the emission of very short-lived nuclei. Values for A_o at the deduced excitation energy $< E_o/A_o >$ *for* each data point were taken from ref. [1] and Z_o was obtained from A_o by requiring the projectile-like prefragment to have the same charge to mass ratio as the projectile. The "chemical potentials", μ_p and μ_n, were treated as free parameters to reproduce the experimental charge distributions.

For the second (decay) stage of the calculation, we focus on the decay of nuclei from both tabulated low lying discrete states[15] and continuum states. Each decay was calculated using tabulated branching ratios where available e[15] and the Hauser-Feshbach formalism [16], when such information is unavailable. Unknown spins and parities of tabulated discrete states were randomly assigned in these

calculations [12,13] and then changed in subsequent calculations to assess the corresponding uncertainties. In general, the uncertainties in R_{HeLi} due to the uncertainties in the unknown spins and parities are of the order of 5%. As the excitation energy is increased into the continuum, the calculations must consider decays of short-lived states with no barrier to particle emission; however, it is likely that many such short-lived states will decay before break up[17-19]. To take this pre-breakup cooling effect into account, we include in the initial population a factor, $\exp(-t_b/t_i)$. Here, $t_i = t(E^*/A)$ is the mean lifetime of the emitted fragment calculated according to the Weisskopf model [21] for statistical decay; t_b is the breakup timescale chosen to be 100 fm/c for this model study. To shorten computation times, an additional constraint $E_i^*/A_o \leq 5MeV$ was imposed on the continuum.

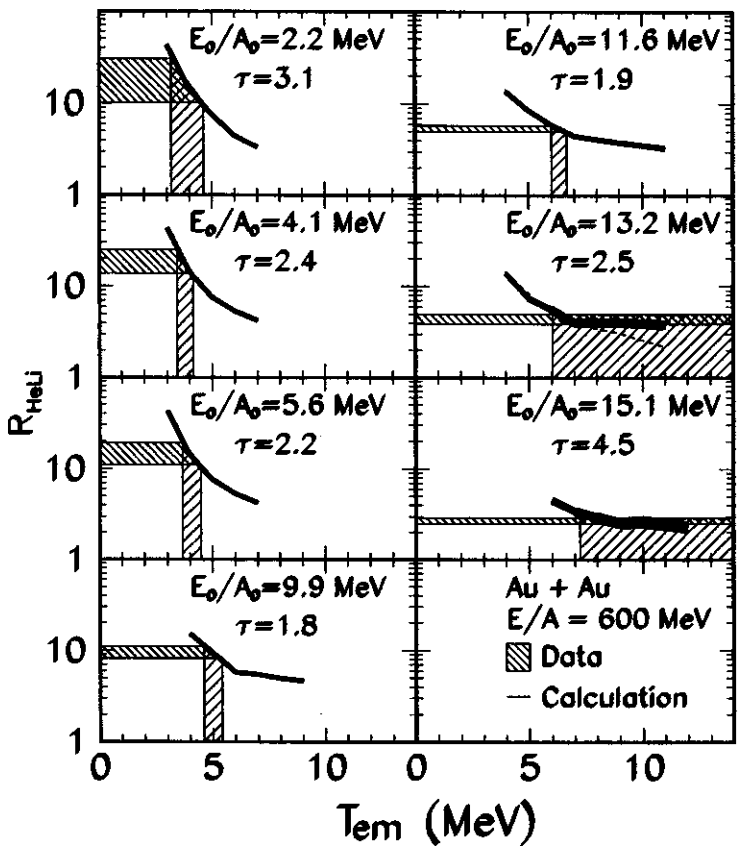

Figure 1: Dependence of the isotope yield ratios as a function of the emission temperature T_{em}, input to the sequential decay calculations. The horizontal hatched areas indicate the measured isotope yield ratios and the vertical shaded areas indicate the range of the extracted isotope temperatures.

Calculations were performed as a function of the emission temperature T_{em} to reproduce the representative experimental data; these data span the range of excitation energies investigated in ref. [1]. The corresponding experimental charge distributions were parameterized by a power law distributions $Y(Z) \propto Z^{-\tau}$ in ref. [22] with τ values given in Figure 1. In our calculations, μ_p and μ_n were not apriori given the values assigned to them as "chemical potentials"[17, 23] or "free excitation energies"[18] within specific statistical models. Instead, they were adjusted to reproduce the measured charge distributions subject to the constraint that the total charge to mass ratio of the emitted particles was consistent with the initial total charge to mass ratio Z_o/A_o. Reproduction of the measured charge distributions is particularly important

when the temperature is large and many excited states are populated since calculated charge distributions that are too steep (too shallow) will underpredict (overpredict) the secondary feeding corrections. Indeed, for the sequential decay calculations *at* $< E_o/A_o >= 13.2$ and 15.1 MeV, changes in τ comparable to the experimental uncertainty of ± 0.5, result in changes of 8-10% in R_{HeLi} for temperature greater than 5 MeV. The solid lines in Figure 1 show the calculated double ratios R_{HeLi} as a function of the emission temperatures, T_{em} . The corresponding values for the excitation energy from ref. [1] and τ from ref. [23] are labeled in each panel of Figure 1. The width of the calculated lines represents the aforementioned 5% uncertainty stemming from the unknown spins and parities of excited states feeding the Helium and Lithium isotopes and also the uncertainty due to the experimental uncertainty of τ. In all calculations, R_{HeLi} flatten out at high temperature, indicating that extremely precise experimental measurements and theoretical calculations would be needed to extract temperatures above $T_{em} > 7$ MeV. If the constraint $E_i^*/A_o \leq 5$ MeV is removed, the calculations become even flatter at $T_{em} > 7$ MeV, and the temperature range for agreement between calculations and data remains unchanged.

a. Department of Physics of Wisconsin, Madison,Wisconsin 53706

References

1. J. Pochodzalla et al., Phys. Rev. Lett. 75, 1040 (1995).
2. D.H.E. Gross, Phys. Rev. Lett. 56, 1544 (1986).
3. J.P. Bondorf, R. Donangelo, I.N. Mishustin, C.J.Pethick, H. Schulz, K.Sneppen, Nucl. Phys. A443 (1985) 321; Nucl. Phys. A444 (1986) 460.
4. M.B. Tsang et. al, Phys. Rev. C53, R1057 (1996).
5. M.B. Tsang, W.G. Lynch, H. Xi, W.A. Friedman, MUSNSCL preprint 1035 (1996).
6. A. Kolomeits et al., Phys. Rev. *C* (in press).
7. X. Campi, H. Krivine, E. Plagnol, Phys. Rev. *C* (submitted).
8. S. Albergo, S.Costa, E.Costanzo, A.Rubbino, Nuovo Cimento 89, 1 (1985).
9. Z. Majka, P. Staszel, J.Cibor, J.B.Natowitz, K.Hagel, J.Li, N.Mdeiwayeh, R.Wada and Y.Zhao, submitted to Phys. Rev. *C*.
10. D. Hahn and H. Stocker, Nucl. Phys. A476, 718 (1988). J. Konopka, H.Graf, H.Stoker, W.Griener, Phys. Rev. C50, 2085 (1994).
11. A. Gilbert, A.G. W. Cameron, Canadian Journal of Physics, 43 (196).
12. T.K. Nayak et al., Phys. Rev. *C* 45, 132 (1992).
13. H.M. Xu et. al., Phys. Rev. *C* 40, 186 (1989) F. Zhu et al., Phys. Rev. *C* 52, 784 (1995).
14. Z. Chen, C.K. Gelbke, Phys. Rev. C38, 2630 (1988).
15. F. Ajzenberg-Selove, Nucl. Phys. A392, 1(1983); A413, (1984); A433, 1 (1985); A449, 1 (1985); A460, 1 (1986).
16. W. Hauser and H. Feshbach, Phys. Rev. 87, 366 (1952).
17. J. Randrup, S.E. Koonin, Nucl. Phys. A356, 223 (1981).
18. W.A. Friedman and W.G. Lynch, Phys. Rev. C28 (1983) 16; (1983) 950.
19. M.G. Mustafa, M. Blann, A.V. Ignatyuk, S.M. Grimes., Phys. Rev. , 1078 (1992).
20. V.F. Weisskopf, Phys. Rev. 52, 295 (1937).
21. C.A. Ogilvie et. al., Nucl. Phys. A553 271c (1993).
22. B.H. Sa, D.H.E. Gross, Nucl. Phys., A437 643 (1985), D.H.E. Gross, X.Z. Zhang, S.Y. Xu, Phys. Rev. Lett., 56, 1544 (1986).
23. J.P. Bondorf, R. Donangelo, I.N. Mishustin, H. Schulz, Nucl. Phys A444, 460 (1985).
24. C. Schwarz et. al. Phys. Rev. *C* 48, 676 (1993) and references .
25. P. Danielewica, Phys. Rev. C51, 716 (1995).

MEASUREMENT OF ISOSPIN DEPENDENCE IN TRANSVERSE FLOW

G.D. Westfall, R. Pak, W. Benenson, O. Bjarki, J.A. Brown, S.A. Hannuschke, R.A. Lacey,[a] Bao-An Li,[b] A. Nadasen,[c] E. Norbeck,[d] P. Pogodin,[d] D.E. Russ,[e] M. Steiner, N.T.B. Stone, A.M. Vander Molen, L.B. Yang,[d] and S.J. Yennello[f]

1. INTRODUCTION

Collective transverse flow can provide information about nuclear reactions at intermediate energy and details of the nuclear equation of state (EOS)[1,2]. One of the most compelling observables related to transverse flow is the incident energy at which the attractive mean field balances the repulsive nucleon-nucleon scattering. This energy is called the balance energy, E_{bal},[3] and can be related to various properties of the EOS through transport models such as the Boltzmann-Uehling-Uehlenbeck (BUU) model. In this paper, we will relate E_{bal} to the in-medium nucleon-nucleon scattering cross sections[4,5].

The beams were produced by the K1200 Superconducting Cyclotron at the National Superconducting Cyclotron Laboratory (NSCL) at Michigan State University (MSU). The MSU 4π Array was used to carry out all the measurements presented here[6].

The main ball of the MSU 4π Array consists of 170 phoswich detectors (arranged in 20 hexagonal and 10 pentagonal subarrays) covering $18° \leq \theta_{lab} \leq 162°$. The 30 Bragg curve counters (BCCs) installed in front of the hexagonal and pentagonal subarrays were operated in ion chamber mode with a pressure of 125 Torr of C_2F_6 gas. The hexagonal anodes of the five most forward BCCs are segmented, resulting in a total of 55 separate ΔE detectors (the BCCs served as ΔE detectors for charged particles that stopped in the fast plastic scintillator of the main ball). Consequently, the main ball was capable of detecting charged fragments from Z = 1 to Z = 16, with mass resolution for the hydrogen isotopes in the phoswiches. Low energy thresholds were approximately 18, 3.5, and 7 MeV/nucleon for fragments with Z = 1, 3, and 12, respectively. In addition to the main ball of the 4π Array, a high rate array (HRA) was also used. The HRA is a close-packed pentagonal configuration of 45 phoswich detectors spanning laboratory polar angles $3° \leq \theta \leq 18°$. With the HRA, Z resolution up to Z=20 and mass resolution for the hydrogen isotopes were obtained.

Data were taken with a minimum bias trigger that required at least one hit in the HRA (HRA-1 data), and a more central trigger where at least two hits in the main ball (Ball-2 data) were required.

2. ISOSPIN DEPENDENCE OF TRANSVERSE FLOW

In this section we demonstrate experimentally that directed transverse flow depends on the isotopic ratio of the system by measurement of flow in three A_{proj} = 58 + A_{targ} = 58 systems with different N/Z at one bombarding energy of 55 MeV/nucleon. Measured flow is stronger for the more neutron-rich system in agreement with BUU predictions [7], which is due mainly to fact that the free neutron-proton cross section is approximately three times higher than the neutron-neutron and proton-proton cross sections at this incident energy. Because most of the experimental conditions (kinematics, available excitation energy, detector configuration, trigger, etc.) were held constant, the change in flow is most likely due to the different N/Z of the three systems. In Fig. 1 we display impact-parameter-inclusive distributions for three global observables from ^{58}Ni+^{58}Ni (solid histograms) and ^{58}Fe+^{58}Fe (dashed histograms) reactions at 55 MeV/nucleon. The left panel shows the total charged-particle multiplicity M_{chgd}; the center panel

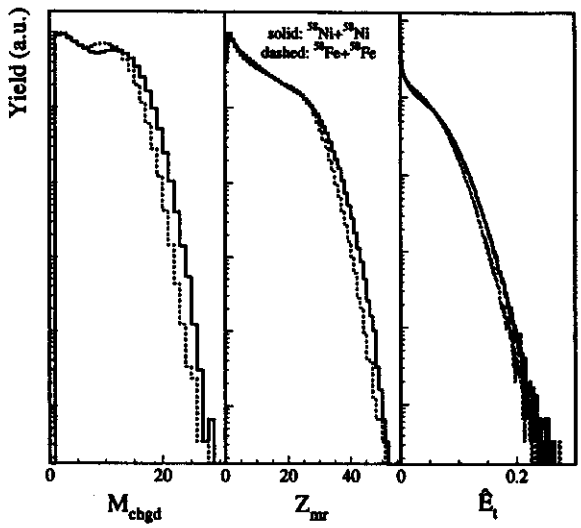

Figure 1: Impact-parameter-inclusive spectra for the total charged-particle multiplicity M_{chgd}, the total midrapidity charge Z_{mr}, and the reduced total transverse kinetic energy $\hat{E}_t$. Solid (dashed) histograms are for ^{58}Ni+^{58}Ni (^{58}Fe+^{58}Fe) collisions at 55 MeV/nucleon.

shows the total midrapidity charge Z_{mr} [8]; and the right panel shows the reduced total transverse kinetic energy $\hat{E}_t$ [9]. These distributions demonstrate that we are comparing similar data sets for these isotopic systems. The impact parameter distributions in the simple geometric picture resulting from the $\hat{E}_t$ spectra in the right panel are nearly identical.

The enhancement at higher values of M_{chgd} and Z_{mr} for central ^{58}Ni+^{58}Ni reactions (Z_{total} = 56) is expected because a larger number of charged particles should be detected than in ^{58}Fe+^{58}Fe reactions (Z_{total} = 52). These fragments would account for a greater amount of participant charge, particularly when the system breaks into many pieces. Presumably these charges would carry off more transverse energy due to greater Coulomb repulsion tending to weaken the isospin effect for the most central collisions. These global variables could not be compared directly for the ^{58}Mn+^{58}Fe system because of poor statistics and some minor contamination (mainly ^{56}Cr) in the secondary beam.

Fig. 2 shows the extracted values of the directed transverse flow for three different fragment types from three different entrance channels plotted as a function of the isotopic ratio of the composite projectile plus target system where $(N/Z)_{sys} = (N_{proj} + N_{targ})/(Z_{proj} + Z_{targ})$. Using this definition we have: $(N/Z)_{sys}$ =1.07 for ^{58}Ni+^{58}Ni; $(N/Z)_{sys}$ =1.23 for ^{58}Fe+^{58}Fe; and $(N/Z)_{sys}$ =1.27 for ^{58}Mn+^{58}Fe.

The data for fragments with Z = 2 and Z = 3 represent the slopes of linear fits over the reduced c.m. midrapidity region -0.5 $\leq (y/y_{proj})_{c.m.} \leq$ 0.5. The fit range was reduced to -0.5 $\leq (y/y_{proj})_{c.m.} \leq$ 0.4 for all three systems for the fits for fragments with Z = 1 because of the presence of a broad peak at projectile rapidity for ^{58}Mn+^{58}Fe not observed in the other systems. The points for Z = 2 from ^{58}Ni+^{58}Ni and ^{58}Mn+^{58}Fe have been offset in value of $(N/Z)_{sys}$ for clarity. The results shown in Fig. 2 demonstrate clearly there is an isospin dependence for directed transverse flow even for the impact-parameter-inclusive data. The neutron-rich system ^{58}Fe+^{58}Fe exhibits larger flow values than ^{58}Ni+^{58}Ni for all three particle types. Although the difference between the flow values extracted for ^{58}Mn+^{58}Fe and ^{58}Fe+^{58}Fe is not statistically significant, the trends are consistent with the reactions involving the two stable beams.

Additional experimental evidence for the isospin dependence of directed transverse flow is shown in Fig. 3. The extracted values of the collective transverse flow in the reaction plane are displayed as a

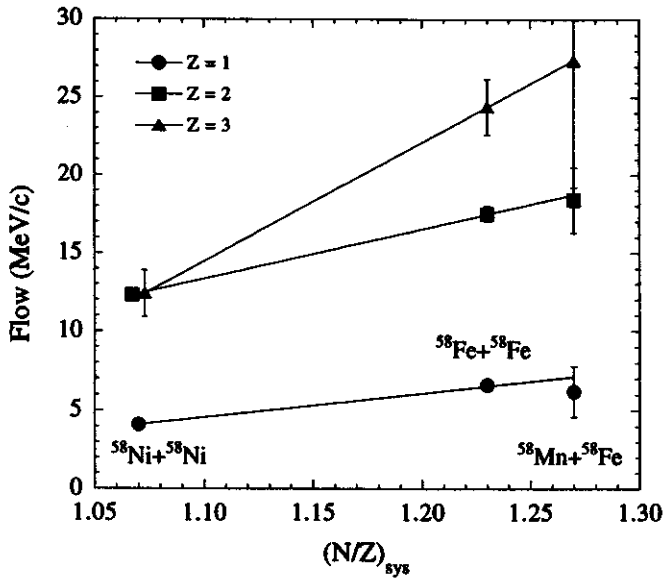

Figure 2: Directed transverse flow as a function of the isotopic ratio of the composite projectile plus target system for three different fragment types from three isotopic entrance channels. The extracted values of the flow are for impact-parameter-inclusive event sets at 55 MeV/nucleon. The lines are included only to guide the eye.

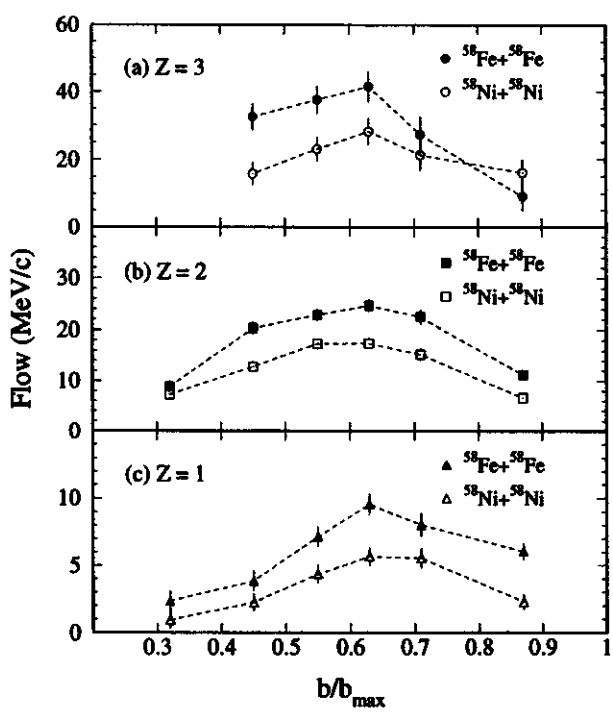

Figure 3: Directed transverse flow as a function of the reduced impact parameter for three different fragment types from ^{58}Fe+^{58}Fe and ^{58}Ni+^{58}Ni collisions at 55 MeV/nucleon. The extracted values of the flow are plotted at the upper limit of each $\hat{b}$ bin. The lines are included only to guide the eye.

function of the reduced impact parameter for three different fragment types from ^{58}Fe+^{58}Fe and ^{58}Ni+^{58}Ni collisions at 55 MeV/nucleon. The extracted values of the flow are plotted at the upper limit of each $\hat{b} = (b/b_{max})$ bin. The errors shown are the statistical errors on the slopes of the linear fits.

The neutron-rich system ^{58}Fe+^{58}Fe systematically exhibits larger flow values than ^{58}Ni+^{58}Ni for all three particle types at all reduced impact parameter bins displayed (except for Z = 3 in the most peripheral bin). The largest difference in the magnitude of the flow between the isotopic entrance channels occurs for heavier mass fragments in semi-central collisions. The impact parameter dependence of the directed transverse flow shown is in qualitative agreement with previous work [2,10,11,12], because the flow is maximal for semi-central events. The mass dependence of the directed transverse flow shown in Fig. 3 also demonstrates the well known increase in magnitude for heavier fragments [2,10,11,13], (note the difference in vertical scale for each panel).

3. ISOSPIN DEPENDENCE OF THE BALANCE ENERGY

In this section we show that E_{bal} depends on the ratio of neutrons to protons (N/Z) of the system by measuring the disappearance of directed transverse flow in two different isotopic systems with different N/Z ratios[4]. Balance energies are larger for the more neutron-rich system at all measured impact parameters in agreement with BUU predictions. Because most of the experimental conditions (kinematics, available excitation energy, detector configuration, trigger, etc.) were held constant, the change in balance energies is due to the different N/Z of the two systems.

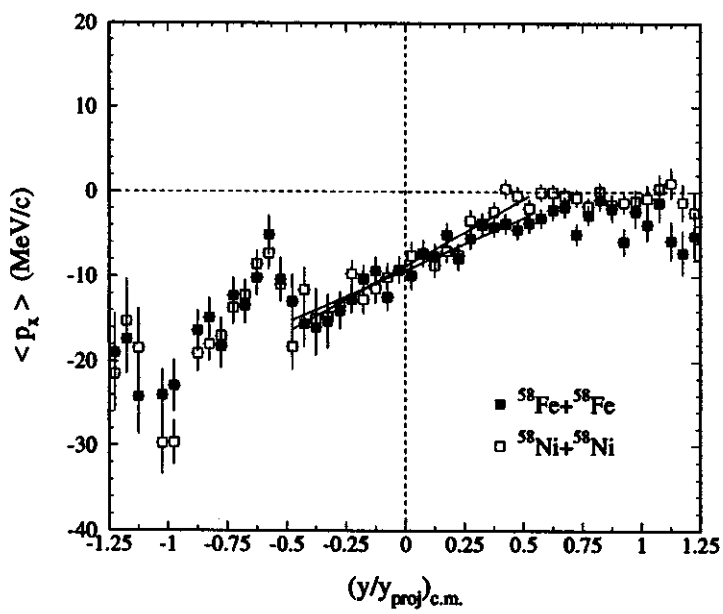

Figure 4: Mean transverse momentum in the reaction plane versus the reduced c.m. rapidity for $Z = 2$ fragments from semi-central collisions (b/b_{max} = 0.48) at 105 MeV/nucleon. The solid (open) squares are for ^{58}Fe+^{58}Fe (^{58}Ni+^{58}Ni). The straight lines are fits over the midrapidity region -0.5 $\leq$ $(y/y_{proj})_{c.m.}$ $\leq$ 0.5.

Fig. 4 shows the mean transverse momentum in the reaction plane $\langle p_x \rangle$ plotted versus the reduced c.m. rapidity $(y/y_{proj})_{c.m.}$ for the two isotopic entrance channels. The solid (open) squares are for fragments with Z = 2 from semi-central ^{58}Fe+^{58}Fe (^{58}Ni+^{58}Ni) collisions at 105 MeV/nucleon. The upper limit of the reduced impact parameter bin for these events is $\hat{b}$ = 0.48. The errors shown are statistical. The only difference between the two data sets is the N/Z ratio of the interacting system. The kinks in the

spectra at $(y/y_{proj})_{c.m.} \approx$ -0.6 are attributed to detector acceptance, but the transverse momentum analysis allows extraction of the flow with as little detector bias as possible [2] by not including affected regions of the spectrum. The vertical offsets from the origin occur because no recoil correction was applied in the reaction plane calculation. This does not affect the final values of the flow observables (balance energies) in this analysis [11]. Each spectrum shown in Fig. 4 is fit with a straight line over the midrapidity region $-0.5 \leq (y/y_{proj})_{c.m.} \leq 0.5$, and the slopes of these lines are defined as the directed transverse flow for each isotopic system. As expected, the directed transverse flow is similar for both isotopic entrance channels, but in what follows the difference is shown to be systematically significant in the data. The extracted values of the directed transverse flow plotted versus the incident beam energy are shown in Fig. 5. The

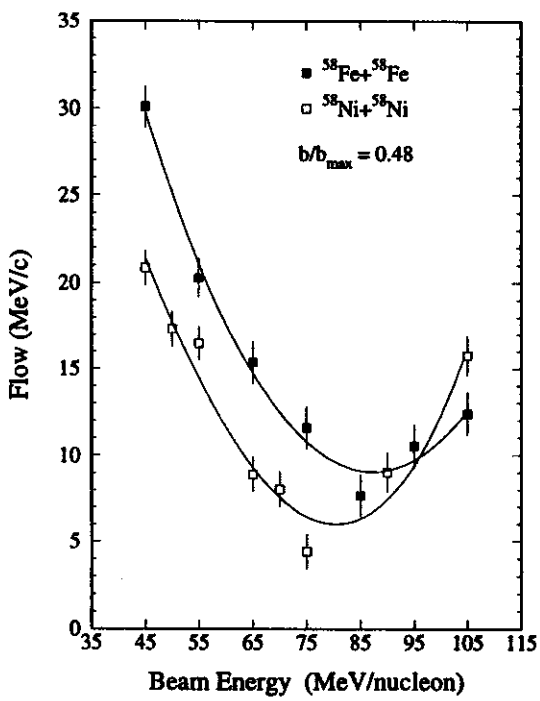

Figure 5: Excitation functions of the measured transverse flow in the reaction plane for $Z = 2$ fragments from semi-central collisions ($b/b_{max} = 0.48$). The solid (open) squares are for ^{58}Fe+^{58}Fe (^{58}Ni+^{58}Ni). The curves are included only to guide the eye.

solid (open) squares are for fragments with $Z = 2$ from semi-central ^{58}Fe+^{58}Fe (^{58}Ni+^{58}Ni) collisions. The errors shown are the statistical errors on the slopes of the linear fits (the systematic error associated with the range of the fitting region is +3 MeV/c and -1 MeV/c). The curves are included only to guide the eye. To extract the balance energy E_{bal}, the data were fit with a second-order polynomial allowing the fitting range to vary until χ^2 per degree of freedom was a minimum [11]. The second-order fits pass through minima for which the value of the abscissa corresponds to the balance energy for that particular entrance channel and $\hat{b}$ bin. The curves do not pass through zero at E_{bal} because no recoil correction was used in the reaction plane determination, as was done elsewhere [10,11]. Collective transverse flow is assumed to be symmetric in the vicinity of the balance energy, and our measurements are unable to distinguish the sign (+ or -) of the flow, so that a local parabolic fit is the lowest order symmetric function that can be used without *a priori* knowledge of E_{bal}.

The horizontal displacement of the minima of the curves in Fig. 5 clearly indicates that E_{bal} is higher for ^{58}Fe+^{58}Fe than ^{58}Ni+^{58}Ni at this $\hat{b}$ bin. That the balance energy is larger for the more neutron-

rich system is primarily attributed to the difference in nucleon-nucleon cross sections [7]. Directed transverse flow has already been shown to be sensitive to in-medium nucleon-nucleon cross sections [13,14]. The neutron-proton cross section is approximately a factor of three higher than the neutron-neutron and proton-proton cross sections over the range of beam energies measured here [7]. This results in less repulsive collective flow from nucleon-nucleon scattering for the more neutron-rich system, pushing the balance energy higher in value.

Below the balance energy the attractive mean field has an even more dominant effect, resulting in higher flow values for the neutron-rich system [4,5]. Above the balance energy where repulsive nucleon-nucleon scattering dominates, the converse is true, resulting in smaller values of the directed transverse flow for the neutron-rich system. Additional experimental evidence for the isospin dependence of the balance energy is presented in Fig. 6. The solid (open) squares are the measured values of the balance

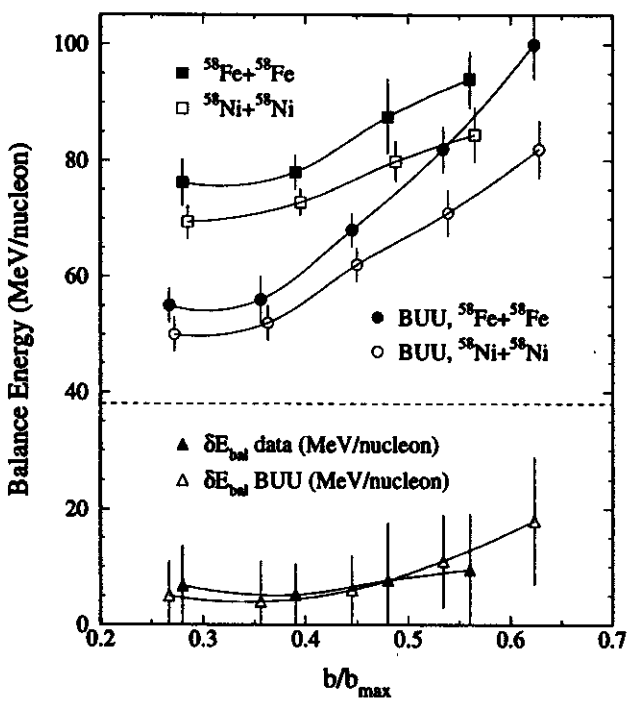

Figure 6: Measured balance energies as a function of impact parameter compared to the predictions of BUU model calculations with an isospin dependent mean field and isospin dependent in-medium nucleon-nucleon cross sections. The solid (open) squares are measured for ^{58}Fe+^{58}Fe (^{58}Ni+^{58}Ni) while solid (open) circles are BUU predictions for ^{58}Fe+^{58}Fe (^{58}Ni+^{58}Ni). The values for ^{58}Ni+^{58}Ni have been offset in the horizontal direction for clarity. The solid (open) triangles correspond to the difference in the balance energies between the isotopic systems at each reduced impact parameter bin for the data (BUU predictions). All curves are included only to guide the eye.

energies for ^{58}Fe+^{58}Fe (^{58}Ni+^{58}Ni) extracted for four reduced impact parameter bins. These experimental values of $E_{bal}(\hat{b})$ are plotted at the upper limit of each $\hat{b}$ bin, and the values for ^{58}Ni+^{58}Ni have been slightly offset in the horizontal direction to show the error bars more clearly. The errors shown on the measured values of the balance energies are statistical. The balance energy increases as a function of impact parameter for both isotopic systems in agreement with previous work [10,12,16], and $E_{bal}(\hat{b})$ is systematically higher for the more neutron-rich system at all measured $\hat{b}$ bins.

The predictions of BUU model [7,15] calculations which incorporate an isospin dependent potential and isospin dependent nucleon-nucleon scattering cross sections for ^{58}Fe+^{58}Fe (^{58}Ni+^{58}Ni) are shown as

solid (open) circles in Fig. 6 for five $\hat{b}$ bins. The errors shown on the calculated points are statistical, and the values for ^{58}Ni+^{58}Ni have been slightly offset in the horizontal direction to show the error bars more clearly. That the balance energy is the same value for all fragment types [11,13] facilitates comparison of the measured values of $E_{bal}(b)$ to predictions of transport models calculations which involve only nucleons. The balance energy has been shown to exhibit little sensitivity to the acceptance effects of our detector array [3], allowing direct comparison between experimental values and unfiltered theoretical results.

The trends in the values of $E_{bal}(b)$ predicted by the BUU model with isospin dependence are consistent with those for the measured values. The balance energy increases as a function of impact parameter for both isotopic systems, and $E_{bal}(b)$ is systematically higher for the more neutron-rich system at all impact parameter bins. That the overall magnitude of the values for the balance energies is underpredicted for central collisions by the BUU model has been attributed to a density dependent reduction of the in-medium nucleon-nucleon cross sections [13,14]. This effect is stronger at smaller impact parameters where the interaction volume is larger than in peripheral collisions. More importantly here, there is agreement between the data and the BUU model predictions for the magnitude of the isospin effect, which is demonstrated explicitly with the lower set of points in Fig. 6. The solid (open) triangles are the difference between the balance energies δE_{bal} for the data (BUU predictions) for the isotopic systems at each corresponding $\hat{b}$ bin. These δE_{bal} values are given in MeV per nucleon and are plotted on the same scale as the values of $E_{bal}(b)$. The errors shown are statistical. There is good agreement between the data and the BUU model predictions for the overall magnitude of δE_{bal}, which is due mainly to the different N/Z ratios of the two isotopic systems. The difference in balance energies between isotopic systems was found to persist for BUU calculations made without Coulomb repulsion, indicating that the isospin effect is mainly due to the difference in the elementary nucleon-nucleon cross sections. The magnitude of δE_{bal} increases for more peripheral collisions where two extended neutron distributions overlap in the reaction of two neutron-rich nuclei [7].

4. CONCLUSIONS

We have demonstrated experimentally that collective transverse flow in nucleus-nucleus collisions depends on the isospin of the system. We used three symmetric systems, ^{58}Fe + ^{58}Fe, ^{58}Ni + ^{58}Ni, and ^{58}Mn+^{58}Fe, at one incident energy to show that flow depends on the isospin of the system. At all impact parmeters and for all observed particle types, flow is larger for the neutron-rich system. In addition, we have measured the balance energy for ^{58}Fe + ^{58}Fe and ^{58}Ni + ^{58}Ni and find that the balance energy is always higher for the neutron-rich system at all impact parameters. BUU calculation reproduce the difference between the two systems. However, BUU underpredicts the observed balance energy in central collisions as was observed previously.

This dependence of the flow on the isospin of the system supports our view of transverse flow as a balance between mostly repulsive nucleon-nucleon scattering and mostly attractive nuclear mean field interactions.

a. Department of Chemistry, State University of New York at Stony Brook, Stony Brook, New York 11794-3400
b. Cyclotron Institute and Department of Physics, Texas A&M University, College Station, Texas 77843-3366
c. Department of Natural Sciences, University of Michigan, Dearborn, Michigan 42128-1491
d. Department of Physics and Astronomy, University of Iowa, Iowa City, Iowa 52242-1479

e. Department of Chemistry and Biochemistry, University of Maryland, College Park, Maryland 20742-2021
f. Cyclotron Institute and Department of Chemistry, Texas A&M University, College Station, Texas 77843-3366

References

1. H. Stöcker and W. Greiner, Phys. Rep. 137, 277 (1986).
2. H.H. Gutbrod, A.M. Poskanzer, and H.G. Ritter, Rep. Prog. Phys. 52, 1267 (1989).
3. C.A. Ogilvie *et al.*, Phys. Rev. C 42, R10 (1990).
4. R. Pak *et al.*, Phys. Rev. Lett. 78, 1022 (1997).
5. R. Pak *et al.*, Phys. Rev. Lett. 78, 1026 (1997).
6. G.D. Westfall *et al.*, Nucl. Instr. and Methods A238, 347 (1985).
7. Bao-An Li *et al.*, Phys. Rev. Lett. 76, 4492 (1996).
8. C.A. Ogilvie *et al.*, Phys. Rev. C 40, 654 (1989).
9. L. Phair *et al.*, Nucl. Phys. A548, 489 (1992).
10. R. Pak *et al.*, Phys. Rev. C 53, R1469 (1996).
11. R. Pak *et al.*, Phys. Rev. C 54, 2457 (1996).
12. J.P. Sullivan *et al.*, Phys. Lett. B 249, 8 (1990).
13. G.D. Westfall *et al.*, Phys. Rev. Lett. 71, 1986 (1993).
14. D. Klakow, G. Welke, and W. Bauer, Phys. Rev. C 48, 1982 (1993).
15. Bao-An Li and S.J. Yennello, Phys. Rev. C 52, R1746 (1995).
16. A. Buta *et al.*, Nucl. Phys. A584, 397 (1995).

DECAY OF TOROIDAL GEOMETRIES

G.D. Westfall, N.T.B. Stone, O. Bjarki, E.E. Gualtieri, S.A. Hannuschke, R. Lacey[a], J. Lauret[a], W.J. Llope[b], D.J. Magestro, R. Pak, A.M. Vander Molen, and J. Yee

1. INTRODUCTION

Recent theoretical calculations based on transport theories have predicted the occurrence of exotic break-up geometries at intermediate energies[1,2,3,4,5,6]. These geometries include bubbles and toroids, which are considered non-compact because of their hollow centers, as well as disks. Experimental searches to date have not been able to confirm these predictions[7,8,9]. Here we present our study of central collisions in the ^{86}Kr+^{93}Nb system at incident energies ranging from 35 to 95 MeV/nucleon. Our results comprise the first systematic experimental results which both provide evidence for the decay of nuclear matter from a toroidal geometry and confine this occurrence to a finite range of beam energies. We use two experimental observables, based on intermediate mass fragment multiplicities and charge similarity, to establish that the system decays from a non-compact break-up geometry. We then use event shape analyses to show that the decaying system is more consistent with a coplanar shape, thus implying that the geometry is toroidal. We find that the toroidal geometries are produced for beam energies between 60 and 75 MeV/nucleon.

This study examines the ^{86}Kr+^{93}Nb system for the beam energies 35, 45, 50, 55, 60, 65, 75, 85, and 95 MeV/nucleon, as produced by the K1200 Superconducting Cyclotron at the National Superconducting Cyclotron Laboratory (NSCL) at Michigan State University (MSU). The experimental data in this study were collected using the MSU 4π Array[10]. Immediately prior to this study, the Array was upgraded, extending the forward coverage for heavy fragments ($Z \leq 27$) down to 0.5° from the beam axis. Sub-arrays forward of 18° have lower energy thresholds of approximately 10 MeV/nucleon for ^{7}Li, and those between 18° and 162° have a corresponding threshold of 3 MeV/nucleon. Although these thresholds prohibit detailed analysis of low-energy kinetic energy spectra, we present below a number of other available experimental signatures.

Our study includes only central events from this data set because the formation of non-compact geometries is predicted for central events[2,4]. We selected central events from our data by using the well-established method of imposing cuts on global observables called centrality variables[11,12]. In order to avoid autocorrelations between the centrality variables and the experimental signatures that we present, we have used two different centrality variables: the total transverse kinetic energy ($E_t = \sum_{i=1,N_c} E_i \sin^2(\theta_i)$), and the total charge of detected fragments traveling at mid-rapidity ($Z_{mr} = \sum_{i,0.75y'_{targ}<y'_{frag,i}<0.75y'_{proj}} Z_i$)[12], where N_c is the number of detected charged particles, E_i is the kinetic energy of each fragment, and y'_{targ}, $y'_{frag,i}$, and y'_{proj} are the center-of-momentum frame rapidities of the target, emitted fragments, and projectile, respectively. To ensure the centrality of the data sample, we applied cuts on E_t accepting only the 5% most central events when dealing with charge-based signatures and similar 5% cuts on Z_{mr} when dealing with the event shape signatures. More stringent event selection (based on *e.g.* fragment emission geometry or alignment) may enhance some predicted signatures at the expense of clarity and generality, but are not needed to establish the signatures shown below.

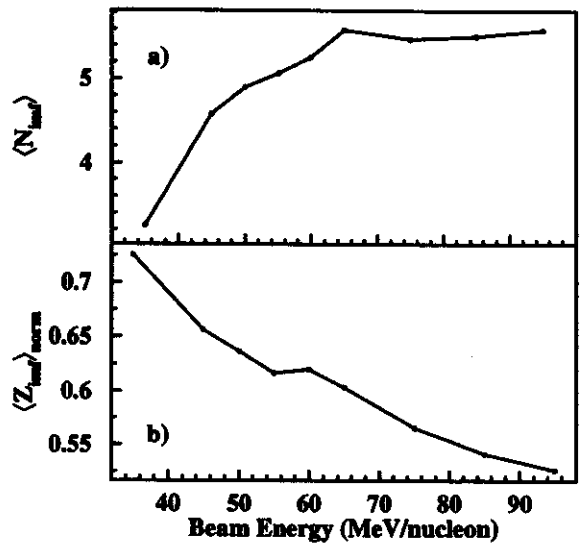

Figure 1: Dependence on the incident beam energy of (a) the mean IMF multiplicity and (b) the total charge of IMFs, normalized by the mid-rapidity charge.

2. IMF MULTIPLICITIES

The first experimental signature we present is an anomalous increase in the number of intermediate-mass fragments (IMFs). An IMF is defined as a fragment with a charge in the range $3 \leq Z \leq 20$. Published percolation model calculations quantitatively demonstrate that decay from non-compact geometries (toroids and bubbles) will result in emission of more IMFs than would be otherwise observed in the decay of a compact spherical geometry[8]. We have measured the multiplicity of IMFs in central events selected via cuts on E_t and plotted the mean values versus the incident beam energy per nucleon in Fig. 1(a). Statistical error bars are smaller than the marker size. Two features are clear in this figure. The first is a general trend in which this multiplicity increases with increasing beam energy. This trend in IMF emission has been documented in previous experimental studies[13,14]. The second feature is an increase in the mean IMF multiplicity which deviates from the more basic trend at a beam energy of 65 MeV/nucleon. Examination of the N_{imf} distributions themselves reveals that this approximate 5% deviation in the mean value is due to a shift in the overall distribution, not to a change in its shape. This qualitative enhancement is consistent with the increase in IMF emission predicted to accompany the formation of non-compact geometries[2,4,8] over a limited energy range, and thus provides our first confirmation.

The enhancement in IMF emission shown in Fig. 1(a) can be further examined by plotting the total charge of detected IMFs divided by the total charge of particles traveling at mid-rapidity ($\langle Z_{imf} \rangle_{norm}$). Because the mid-rapidity charge roughly corresponds to the size of the emitting source, in this way we divide out the (changing) size of the source and obtain a normalization for the amount of the system emitted as IMFs. This quantity is plotted in Fig. 1(b), and shows an overall trend consistent with the decreasing prevalence of charge bound in IMFs. It also shows a 5% enhancement reminiscent of the IMF multiplicity enhancement shown in Fig. 1(a), although at a slightly lower energy. We shall return to this latter point at length. This enhancement is also due to a shift in the distributions and not to a change in their shape. Thus, we observe the enhancement signature in IMF emission even when factoring in the

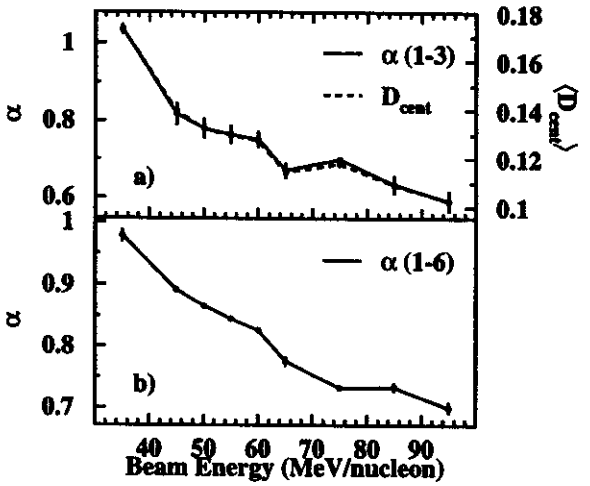

Figure 2: Dependence on the incident beam energy of extracted α values (solid lines) calculated using only the largest (a) three fragments and (b) six fragments. Also in (a), the dashed line shows extracted values of D_{cent}.

increasing size of the emitting system.

3. CHARGE SIMILARITY

The second signature we present is an enhanced similarity in the charges of large fragments. Some theoretical models have quantitatively predicted that the formation of non-compact geometries will also result in increased cross sections for the emission of fragments with nearly equal masses[4,15]. To quantify this phenomenon for our data, we have calculated the power-law exponents for ordered Z distributions. This calculation begins with the ordering of the charges of the detected fragments, from largest to smallest, on an event-by-event basis. In this way, each fragment is assigned an index from 1 to N_c, the total number of charged particles. We then calculate the mean charge for each of these indexed charges over all events in our sample. We have observed empirically that these ordered Z distributions are best reproduced by a power-law (*i.e.* $\langle Z_{ord}(i) \rangle \propto i^{-\alpha}$), although the qualitative features of the signature we present below are insensitive to the fit type. It follows that the fit parameter α for these distributions would be small for events which contain very similarly charged fragments, and large for events which contain very differently charged fragments. Thus, the presence of a non-compact break-up geometry giving rise to more similarly charged large fragments should be accompanied by a suppressed value of this exponent.

We have extracted the power-law exponent α for central events selected via cuts on E_t and plotted them versus the beam energy as solid lines in Fig. 2(a). Statistical errors are smaller than the markers, and systematic fitting errors are plotted. We observe an overall trend in α, decreasing with increasing beam energy, corresponding to an increasing probability for the emission of IMFs having similar sizes. It is clear that this observable, like the IMF multiplicity, also undergoes a (5%) departure from the overall smooth trend, and at a similar beam energy.

The solid lines depict those values obtained by fitting only the 3 largest charges in each event. These are compared directly to another quantitative measure of charge symmetry ($\langle D_{cent} \rangle$) obtained from Dalitz plots (Ref. 16). D_{cent} is defined as the distance from the center of a Dalitz triangle to the coordinates calculated from the charges of the 3 largest fragments in each event, such that small values of D_{cent} correspond to events having similar charges, and large values correspond to dissimilar charges. The

comparison of the mean values of D_{cent}, shown by dashed lines, to those obtained for α, shown by solid lines, illustrates that our method of using ordered-charge distributions reproduces the results of other well-known charge similarity observables. However, the advantage to the latter method is that it can be applied to an arbitrary number of particles.

Because we have established (Fig. 1(a)) that $\langle N_{imf} \rangle \sim 5.5$ for this system, we have extracted the exponent α by fitting the first 6 charges (Fig. 2(b)). The reduction in systematic error resulting from the inclusion of a broader fit range is also evident from this figure. In this case, the extracted α values at 65 and 75 MeV/nucleon are suppressed so that they lie below the values consistent with the overall smoothly decreasing trend. This suppression in α (and in D_{cent}) is an indication of more equally sized large fragments and has been predicted to accompany the formation of non-compact geometries[4]. By comparing Fig. 2, frames (a) and (b), we show again that the precise energies of this phenomenon are slightly different, and depend somewhat on the details of the definition of the observables.

Based on these quantitative and qualitative predictions, the two charge-based observables shown above (multiplicity and similarity) demonstrate trends that are well explained by the decay of non-compact geometries. However, to differentiate between the possibilities of toroid and bubble formation an additional signature is required. The use of event shape observables to make precisely this distinction was proposed by the authors of Ref. 4.

4. EVENT SHAPE

The third signature we present is a suppressed sphericity in the emission of heavy fragments. It is derived from the sphericity of particle emission in momentum space, and it ascribes a quantitative measure to the dimensionality of the break-up geometry. Such an observable includes all of the information measured for each fragment (*i.e.* charge, energy, emission angles), and thus provides a good balance to observables based on charges alone. Sphericity is defined[17] by first generating the kinetic energy tensor such that $T_{ij} = \sum_{n=1}^{N_{imf}} (p_{i,n} p_{j,n})/2m_n$ where N_{imf} is the number of IMFs in each event, and $p_{i,n}$ and m_n are the i^{th} component of the momentum and the mass of each IMF, respectively. Next, the eigenvalues (λ_i) of this tensor are calculated, ordered ($\lambda_1 > \lambda_2 > \lambda_3$), and normalized ($q_i = \lambda_i / \sum_{j=1}^{3} \lambda_j$), and the sphericity is defined as $S = \frac{3}{2}(q_2 + q_3)$. Given this definition, events with isotropic emission of IMFs will have a high value of sphericity, while those with coplanar or otherwise non-spherical emission will have lower values. It is known that the range of allowed values of sphericity is affected by the multiplicity of particles (N_{imf}) in the tensor sum. To account for this effect, we compare events having the same IMF multiplicities[18]. We will also extract from this tensor the flow angles ($\cos(\theta_i)$) which correspond to the alignment of each of the eigenvectors and are obtained directly via the dot product of the eigenvectors with the z-axis. By the ordering of eigenvalues described above, θ_1 thus corresponds to the azimuthal angle of the eigenvector associated with the largest eigenvalue.

We have calculated the mean values of the sphericity of IMF emission ($\langle S \rangle$) for central events selected via cuts on Z_{mr} and plotted these (markers) versus the incident beam energy per nucleon for one representative IMF multiplicity ($N_{imf} = 5$) in Fig. 3(a). The trends observed for other multiplicities are nearly identical to those shown. Statistical errors on the mean values are smaller than the marker size and systematic errors are shown. We have plotted above and below the values obtained from the experimental data the resulting mean values obtained from the output of an event generator[19] which produced spherical (dotted lines) and disk-like (dot-dashed lines) emission patterns. The significant input parameters to this model were the aspect ratio of the ellipsoid of particle emission, the emission source

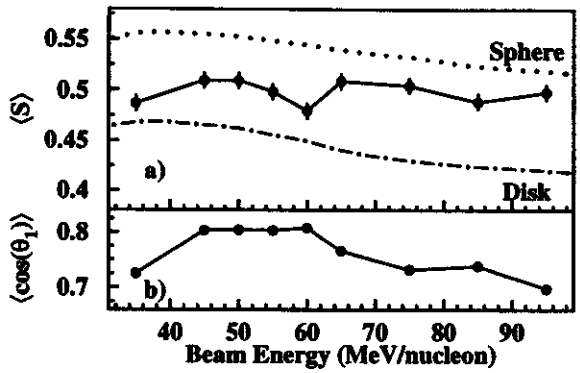

Figure 3: Dependence on the incident beam energy of the measured (a) mean sphericity of IMF emission (markers) and (b) cosine of the flow angle corresponding to the largest eigenvalue. Also in (a), the dotted and dot-dashed lines indicate the mean values obtained for filtered spherical and disk-like simulations, respectively.

temperature, and charge and multiplicity distributions. The aspect ratios used were 1:1:1 and 2.5:2.5:1 for the sphere and disk simulations, respectively, and source temperatures were extracted from relativistic Maxwell-Boltzmann fits to experimental energy spectra for Z=3 (the smallest IMF) fragments. Charge and multiplicity distributions were constrained to match the observed experimental distributions resulting in central events. The output from this model was then filtered through a detailed software replica of our detector which accounted for effects such as upper and lower kinetic energy thresholds, uncovered solid angle, malfunctioning detectors, and multiple particle hits. Thus we can compare the sphericity values for these simulated emission patterns directly to our experimental data.

The sphericity values resulting from the disk-like simulation are lower than those resulting from the spherical simulation. This difference illustrates the effectiveness of sphericity in quantitatively distinguishing disk-like emission from spherical emission. Second, an examination of the excitation function of the sphericity values yielded by the filtered simulation reveals that changes in the acceptance effects on $\langle S \rangle$ with increasing beam energy are smooth, so that any significant change in the experimental data that does not follow this smooth trend cannot be attributed to systematic changes in acceptance.

The experimental values of sphericity fall between the limiting values obtained for the spherical and disk-like simulations, and the shape of the curve reflects the same basic trends which we associate here with acceptance effects. However, at a beam energy of 60 MeV/nucleon, the experimental value of $\langle S \rangle$ is suppressed by 5%, approaching the disk-like values. This suppression, reflecting a shift in the sphericity distributions, cannot be attributed to experimental acceptance and is beyond statistical fluctuations, indicating more disk-like, or coplanar, IMF emission at this energy. The value of sphericity achieved at 60 MeV/nucleon is consistent with a disk of aspect ratio 2:2:1. Parallel analysis of other event shape observables (*e.g.* coplanarity) reveals corresponding suppression/enhancement signatures at the same beam energy. This trend shown in the event shape observables confirms the occurrence of a more two-dimensional break-up geometry.

In the case of toroid formation (*cit.* Ref. [2]), the torus is oriented perpendicular to the beam axis. Thus a perfectly central collision would give rise to two comparatively large eigenvalues with eigenvectors perpendicular to the beam axis, so that the three signatures presented above would be further corroborated by a suppression in the cosine of the first flow angle ($\cos(\theta_1)$, as previously defined). The mean value of this cosine is plotted in Fig. 3(b), and does show a suppression, although at a slightly different energy than

that shown in Fig. 3(a). This transition to a more perpendicular orientation is the fourth independent signature we present as evidence for the decay of toroidal geometries.

The subtle and recurring variation in the energy of toroidal breakup as presented in this report suggests a variation in the sensitivities of specific observables, dependent upon their definitions. These differences prohibit the precise location of a transitional beam energy and merits further inquiry. However, all observables exhibit sensitivity to the occurrence of this phenomenon and together form strong experimental support for the formation of toroidal geometries.

5. CONCLUSIONS

We have presented a systematic study of four independent global experimental observables for the ^{86}Kr+^{93}Nb system for incident energies ranging from 35 to 95 MeV/nucleon. Our study reveals a 5% enhancement in emission of intermediate-mass fragments (IMFs) and in similarity in the charges of these large fragments, which together establish the non-compact nature of the break-up geometry. We also observe a 5% suppression in the mean value of the sphericity and suppressed flow angles of IMF emission, which indicate toroidal, as opposed to bubble-like, geometries. All of these signatures occur at energies between 60 and 75 MeV/nucleon. These signatures are predicted by many of the same theoretical models that have provided us with the most recent descriptions of non-compact geometries, and should be interpreted in that context as experimental evidence for the existence of toroidal break-up geometries.

We gratefully acknowledge the assistance of J. Svoboda in the data reduction.

a. Department of Chemistry, State University of New York at Stony Brook, Stony Brook, New York 11794
b. T.W. Bonner Nuclear Laboratory, Rice University, Houston, TX 77251

References

1. L.G. Moretto *et al.*, Phys. Rev. Lett. 69, 1884 (1992).
2. W. Bauer, G.F. Bertsch, and H. Schulz, Phys. Rev. Lett. 69, 1888 (1992).
3. D.H.E. Gross, B.A. Li, and A.R. DeAngelis, Ann Phys. (Leipzig) 1, 467 (1992).
4. H.M. Xu *et al.*, Phys. Rev. C 48, 933 (1993).
5. S.R. Souza and C.Ngô, Phys. Rev. C 48, R2555 (1993).
6. A. Guarnera *et al.*, GANIL Preprint P95-05, (1995).
7. T. Glasmacher, C.K. Gelbke, and S. Pratt, Phys. Lett. B 314, 265 (1993).
8. L. Phair, W. Bauer, and C.K. Gelbke, Phys. Lett. B 314, 271 (1993).
9. L.G. Moretto *et al.*, Phys. Rev. Lett. 77, 2634 (1996).
10. G.D. Westfall *et al.*, Nucl. Inst. Meth A238, 347 (1985).
11. C. Cavata *et al.*, Phys. Rev. C 42, 1760 (1990).
12. L. Phair *et al.*, Nucl. Phys. A548, 489 (1992).
13. G.F. Peaslee *et al.*, Phys. Rev. C 49, R2271 (1994).
14. W.J. Llope *et al.*, Phys. Rev. C 51, 1325 (1995).
15. C.Y. Wong, Ann. Phys. 77, 279 (1973).
16. N.T.B. Stone *et al.*, Phys. Rev. C 51, 3157 (1995), and references therein.
17. G. Fái and J. Randrup, Nucl. Phys. A404, 551 (1983).
18. W.J. Llope *et al.*, Phys. Rev. C 52, 1900 (1995).
19. E.E. Gualtieri, Ph.D. Dissertation, Michigan State University, 1995 (Unpublished).
20. J. Cugnon and D. L'Hote, Nucl. Phys. A397, 519 (1983).

AZIMUTHAL 2α-CORRELATIONS AND PROJECTILE-RESIDUE DISTRIBUTIONS SELECTED BY NEUTRON AND CHARGED-PARTICLE MULTIPLICITY MEASUREMENTS

G.J. Kunde, S.J. Gaff, C.K. Gelbke, T. Glasmacher, M.J. Huang, R. Lemmon, W.G. Lynch, L. Manduci, L. Martin, M.B. Tsang, W.A. Friedman[a], J. Dempsey[b], R.J. Charity[b], L.G. Sobotka[b], D.K. Agnihotri[c], B. Djerroud[c], W.U. Schröder[c], W. Skulski[c] J. Töke[c], K. Wyrozebski[c], and D. Ruess[d]

For energetic nucleus-nucleus collisions, many experimental observables are predicted to exhibit a strong dependence upon impact parameter [1]. Reaction models are therefore most sensitively tested by "exclusive" experiments which provide reaction filters capable of selecting events according to narrow ranges of impact parameters. For intermediate-energy nucleus-nucleus collisions, such a selection is often obtained from the multiplicity of emitted neutrons or charged particles [2]. Only limited information about the relative selectivity of various reaction filters is available [4-9], and no quantitative comparison of neutron and charged-particle multiplicity filters exists.

A number of examples underline the the importance of a comparison of event selection based upon neutron and charged particle multiplicity measurements. Very similar neutron multiplicity (N_N) distributions were observed in Ar + Au (and Th) collisions at E/A = 44 and 77 MeV [10]. However, over the energy range E/A = 35-110 MeV, the multiplicity distribution of charged particles (N_C) was observed to extend to higher values of N_C with increasing beam energy [11]. Experiments with ^{136}Xe + ^{209}Bi at E/A = 28 MeV [12,13] and ^{197}Au + ^{197}Au at E/A = 35 MeV [14,15], selected by cuts on N_N and N_C respectively, found different numbers of sources for IMF emission. Thirdly a comparison between neutron and charged-particle multiplicity filters revealed higher multiplicities of intermediate mass fragments (IMF) when central Sn+Sn collisions were selected by cuts on N_C than when selected by cuts on N_N [16]. These observations raise the question whether the selection of small impact parameters by cuts on N_N provides a resolution comparable to that provided by cuts on N_C.

Examination of other observables with a strong impact parameter dependence, such as the azimuthal distribution of α-particles emitted at intermediate rapidity [9] or the charge distribution of projectile-like fragments (PLF) emitted at small angles, can provide information about the relative resolution of the two reaction filters. The relationship between impact parameter and emitted particle multiplicity was optimized by studying , symmetric reactions [1]. To explore the sensitivity to the N/Z ratio of projectile and target, we performed measurements for ^{112}Sn + ^{112}Sn and ^{124}Sn + ^{124}Sn, at a beam energy of E/A = 40 MeV. The beams were accelerated by the K1200 cyclotron and irradiated targets of $5mg/cm^2$ areal density. For each event, the associated neutron multiplicity was measured with the SuperBall neutron multiplicity meter [17], the largest device of its kind currently available. The neutron-detection efficiency was estimated [17] to be approximately 80% for emission from a target-like source, 50% for emission from a projectile-like source, and 65% on average. Coincident charged particles were measured with 280 plastic scintillator - CsI(Tl) phoswich detectors of the Miniball/Miniwall array [18,19] mounted in the Superball scattering chamber. The charged particle array covered approximately 90% of 4π.

Projectile-like fragments with $Z \geq 15$ were detected in a Si-CsI(Tl) array (300 μm Si and 20 mm CsI) covering the angular range of $2.4° \leq \Theta_{lab} \leq 5.4°$. The event trigger required the detection of at least two charged particles in the Miniball/Miniwall array.

Multiplicity distributions of detected charged particles (N_C) and neutrons (N_N) are shown in the

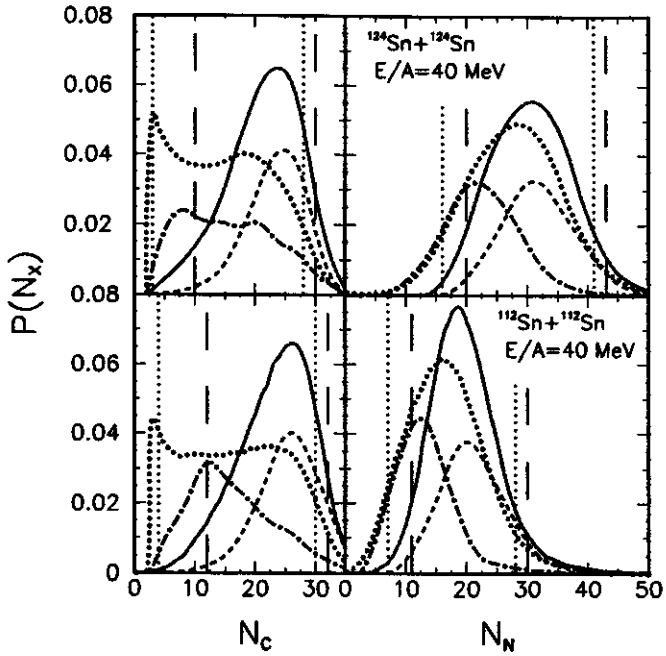

Figure 1: Charged-particle (N_C, left panels) and neutron (N_N, right panels) multiplicity distributions measured for the event trigger (dotted curves) and with the additional requirement of detecting two coincident α-particles at $25° \leq \Theta_{lab} \leq 60°$ (solid curves). Top and bottom panels show results for $^{124}Sn + ^{124}Sn$ and $^{112}Sn + ^{112}Sn$, respectively. Dot-dashed and dashed curves show N_C (N_N) distributions selected by peripheral and central cuts on N_N (N_C). Peripheral and central cuts are indicated by long-dashed vertical lines; they delimit the upper and lower 5% of the areas under the solid curves.

left and right panels of Fig. 1; top and bottom panels are for $^{124}Sn + ^{124}Sn$ and $^{112}Sn + ^{112}Sn$. Dotted and solid curves show distributions measured in coincidence with the event trigger and in coincidence with two α- particles detected at $25° \leq \Theta_{lab} \leq 60°$. For ease of presentation, these two curves are normalized to unit area. The event trigger suppresses low neutron-multiplicity events corresponding to the most peripheral collisions for which few charged particles are emitted. An additional, more significant suppression of peripheral events is imposed by the requirement the 2α- requirement – as needed for the construction of the azimuthal correlation functions discussed below (see solid curves). The left (right) long-dashed vertical lines delimit the upper (lower) multiplicity boundaries for the peripheral (central) collision gates which delimit the lower (upper) 5% of the areas under the solid curves. The dotted vertical lines show analogous 5% cuts for the event trigger (used in Fig. 4) without the 2α-coincidence requirement.

The dashed and dot-dashed curves show the shapes of the N_N (N_C) distributions selected by central and peripheral cuts on N_C (N_N). Narrow cuts on N_C produce rather broad distributions in N_N and vice versa – corresponding cuts on N_C and N_N select different, though somewhat overlapping classes of events.

The dashed and dot-dashed curves show the shapes of the N_N (N_C) distributions selected by central and peripheral cuts on N_C (N_N); for ease of presentation, these curves were normalized to subtend an area of 0.5. Narrow cuts on N_C produce rather broad distributions in N_N and vice versa – thus corresponding cuts on N_C and N_N select different, though somewhat overlapping classes of events.

In order to explore the selectivity of cuts on N_C and N_N, we investigate the shapes of azimuthal $\alpha - \alpha$ correlation functions which have been shown to strongly correlate with various reaction filters [9]. For the reactions considered here, these correlations are dominated by a rotational motion which produces a characteristic "V-shape" of the azimuthal correlation function [9,20,23]. The azimuthal $\alpha - \alpha$ correlation functions are defined as

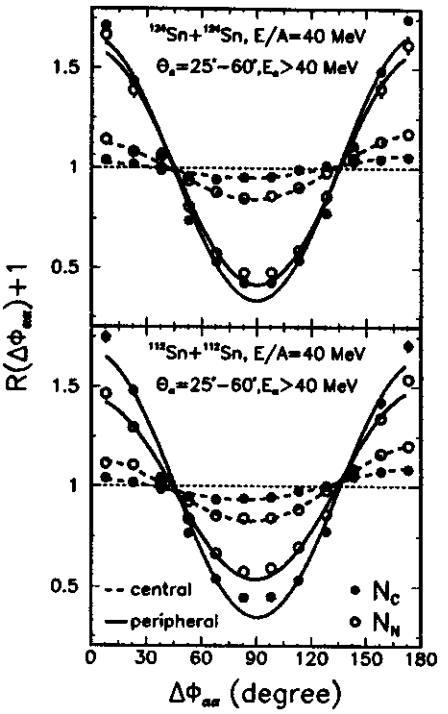

Figure 2: Azimuthal $\alpha-\alpha$ correlation functions observed for central and peripheral cuts on N_N (open points) and N_C (solid points). Top and bottom panels show results for ^{124}Sn + ^{124}Sn and ^{112}Sn + ^{112}Sn, respectively. Solid and dashed curves show fits (with Eq. 2) to correlations selected by peripheral and central cuts, respectively.

$$1 + R(\Delta\phi_{\alpha\alpha}) = \frac{\sum Y_{\alpha\alpha}(\theta_1, \phi_1, \theta_2, \phi_2)}{Y_{\rm back}(\theta_1, \phi_1, \theta_2, \phi_2)}. \quad (1)$$

Here $Y_{\alpha\alpha}(\theta_1, \phi_1, \theta_2, \phi_2)$ is the coincidence yield for the detection of two α-particles at polar and azimuthal angles θ_i and ϕ_i $(i = 1, 2)$ and $Y_{\rm back}(\theta_1, \phi_1, \theta_2, \phi_2)$ denotes the "background" yield constructed by the event mixing technique. The sum in Eq. 1 extends over all pairs of α-particles within a given bin of $\Delta\phi_{\alpha\alpha} = |\phi_1 - \phi_2|$ (defined over the interval $[0°, 180°]$) and with $25° \leq \Theta_{lab} \leq 60°$. The cut on Θ_{lab} selects α-particles emitted at approximately $90° \pm 30°$ in the center-of-mass system. To reduce possible many-body Coulomb distortions for particles emitted at very low energy and eliminate small-angle distortions from the decay of particle-unstable ^{8}Be-nuclei, the summation were further constrained by $E_{\alpha,\rm lab} > 40$ MeV and $E_{\rm rel} > 250$ keV, where $E_{\rm rel}$ is the kinetic energy in the $\alpha - \alpha$ center-of-momentum system.

Figure 2 shows $\alpha - \alpha$ correlation functions, selected by the peripheral and central cuts on N_C and N_N defined in Fig. 1. Top and bottom panels show results for ^{124}Sn+ ^{124}Sn and ^{112}Sn + ^{112}Sn. Consistent with previous results [9,22], much stronger V-shaped correlations are observed for peripheral than for central, violent collisions. For peripheral ^{112}Sn + ^{112}Sn collisions, the V-shape of the $\alpha - \alpha$ correlation function is more pronounced for the cut on N_C than on N_N, but for peripheral ^{124}Sn+ ^{124}Sn collisions, the two cuts produce very similar correlation functions. Since ^{124}Sn+ ^{124}Sn collisions are associated with higher neutron multiplicities, this qualitative difference between the two reactions could be due to a difference in impact-parameter resolution for the peripheral cuts on N_N. For ^{124}Sn+ ^{124}Sn, peripheral cuts on N_N and N_C appear to have comparable resolution, but for the ^{112}Sn + ^{112}Sn reaction cuts on N_C appear to provide better selectivity than cuts on N_N. For both reactions, the $\alpha - \alpha$ correlation functions are more isotropic for the central cut on N_C than on N_N.

For a more quantitative discussion [9], we have fit the measured $\alpha - \alpha$ correlation functions with

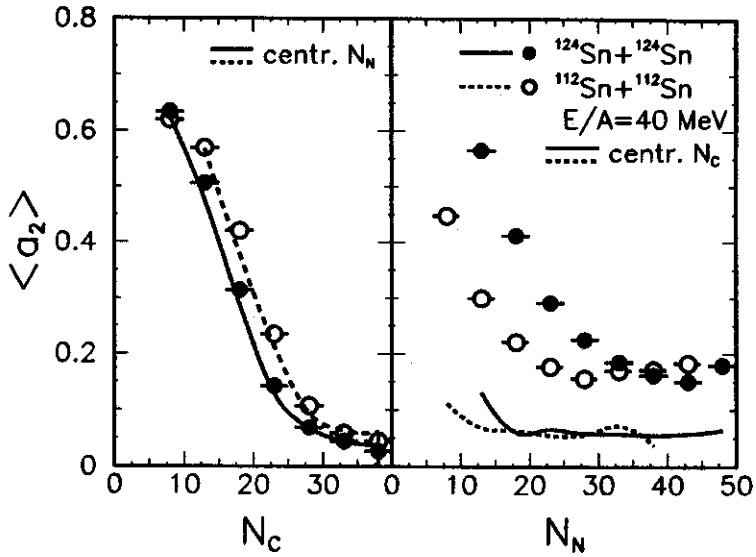

Figure 3: Dependence of fit parameter a_2 (see Eq. 2) on N_C and N_N. The curves show the dependences on N_C (N_N) for central collisions selected by a cut on N_N (N_C). Solid points and solid curves (open points and dashed curves) indicate results for ^{124}Sn + ^{124}Sn (^{112}Sn + ^{112}Sn).

the functional form [9,22,23]

$$1 + R(\Delta\phi_{\alpha\alpha}) = a_0(1 + a_1 \cos\Delta\phi_{\alpha\alpha} + a_2 cos2\Delta\phi_{\alpha\alpha}), \tag{2}$$

where the parameters a_1 and a_2 provide a measure for sideward directed and rotational flow, respectively [23]. Representative fits are shown by the curves in Fig. 2. Parameters a_2 characterizing azimuthal $\alpha - \alpha$ correlation functions selected by different cuts on N_C and N_N are shown in the left and right panels of Fig. 3. Open and solid points show the results for ^{112}Sn + ^{112}Sn and ^{124}Sn+ ^{124}Sn , respectively. The reduced range of variation of a_2 for cuts on N_N (as compared to cuts on N_C) strongly suggests event selection with reduced resolution. The curves in the left (right) panels show the variation of a_2 as a function of N_C (N_N) when the events are further restricted by central cuts on N_N (N_C). Rather surprisingly, a central cut on N_N has little effect on the N_C- dependence, but a central cut on N_C essentially defines a_2 with little further dependence on N_N. The shape of the azimuthal $\alpha - \alpha$ correlation functions thus is well determined by cuts on N_C; additional constraints on N_N have little if any effect.

If one assumes that the shape of the $\alpha - \alpha$ correlation function is primarily determined by the impact parameter of the collision, then one is led to the conclusion that the impact parameter is better determined by cuts on N_C than on N_N and that, further, an additional cut on N_N does not improve the impact parameter selection. It is, however, conceivable that many-body Coulomb final- state interactions could attenuate the original emission pattern, thus leading to decreasing values of a_2 as a function of N_C, but not N_N, for a fixed impact parameter. While an accurate determination of final-state Coulomb distortions requires knowledge of the complete many-body emission function, we have estimated their possible importance via many-body Coulomb trajectory calculations [25], assuming an instantaneous release of all charged particles from the surface of a hot rotating gas, modeled as in ref. [20]. Specifically, we used a realistic element distribution and source parameters [20], $(R_{w/c}, T)$ = (0.08, 10 MeV) and (0.1, 5 MeV), adjusted to provide an approximate description of the average α-particle energy spectrum and to produce azimuthal $\alpha - \alpha$- correlations comparable to those measured. For simplicity, all particles were

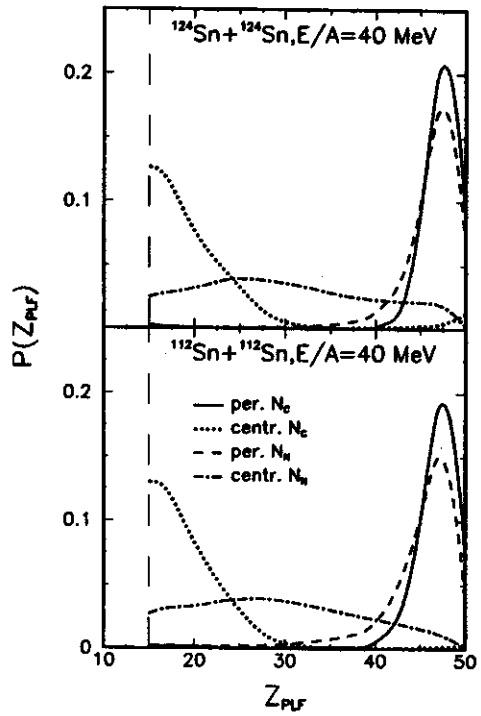

Figure 4: Charge distributions of projectile-like fragments detected at $2.5° \leq \Theta_{lab} \leq 5.4°$ for events selected by peripheral and central cuts on N_C (dotted and solid curves) or N_N (dashed and dot-dashed curves). Top and bottom panels show results for ^{124}Sn + ^{124}Sn and ^{112}Sn + ^{112}Sn, respectively. The long-dashed vertical lines indicate the projectile-like fragment detection threshold.

treated as point particles moving under the influence of their mutual Coulomb forces. This ansatz is likely to overestimate the effect of final-state Coulomb interactions due to the assumed compact initial geometry and the neglect of finite emission times. For such an extreme scenario, we found that many-body Coulomb interactions could reduce the unperturbed values of a_2 by up to 50% for $N_C = 40$. While significant, the calculated distortions could not account for the observed variation of a_2 with N_C (by a factor of eight) when central collisions are selected by N_N.

An alternative observable expected to strongly correlate with impact parameter is the Z-distribution of projectile-like fragments (PLF) observed at forward angles. Figure 4 compares PLF element-distributions detected in the forward array and selected by central and peripheral cuts on N_C (solid and dotted curves, respectively) and N_N (dashed and dot-dashed curves, respectively). In this particular case, the 2α-coincidence restriction is unnecessary; thus central and peripheral cuts represent 5 % of the normal event trigger yields (shown by the dotted curves in Fig. 1). The PLF distributions selected by cuts on N_C are narrower than those selected by cuts on N_N . For peripheral cuts, this difference may be less significant, but for central cuts this difference is large, suggesting much improved impact parameter selection by central cuts on N_C.

Qualitatively, a superior impact parameter selectivity of reaction filters based on charged-particle multiplicity may be explained in a simple participant spectator picture. Very peripheral "binary" collisions produce large numbers of thermal neutrons, but very few charged particles. This large thermal neutron multiplicity may present a "background noise" which washes out the impact parameter sensitivity for more violent collisions for which energetic neutrons and charged particles are emitted from overlap zone between projectile and target. For charged particles, on the other hand, the background from peripheral collisions is small. Further, energetic charged particles emitted from the overlap zone are detected with higher efficiency than neutrons. The combination of these effects could lead to an improved N_C signal as

soon as the overlap between projectile and target becomes appreciable.

In summary, we studied symmetric collisions of ^{112}Sn + ^{112}Sn and ^{124}Sn + ^{124}Sn, with combined 4_{π}-detection capability for neutrons and charged particles. We found strong evidence that better impact parameter selectivity is provided by cuts on charged particle multiplicity than by cuts on neutron multiplicity, at least over the small to mid impact-parameter range associated with significant charged particle emission. This observation does not preclude the possibility that a judicious combination of charged-particle and neutron- multiplicity information might allow an additional constraint on the total dissipated energy –which is expected to fluctuate even for a collisions at a fixed impact parameter. However, an experimental proof-in-principle for this latter possibility still needs to be established.

a.Department of Physics, University of Wisconsin, Madison, WI 53706, USA
b.Department of Chemistry, Washington University, St. Louis, MO 63130, USA
c.Department of Chemistry and Nuclear Structure Research Laboratory, University of Rochester, Rochester, NY 14627, USA
d.Department of Chemistry, University of Maryland, College Park, MD 20742, USA

References

1. M.B. Tsang et al., Phys. Rev. C40,1685 (1989).
2. J. Galin et al., J. Phys. G: Nucl. Part. Phys. 20. 1105 (1994).
3. L.G. Moretto et al., Ann. Rev. Nucl. Part. Sci. 43, 37 (1993), and references therein.
4. J. Galin et al., Z. Phys. A331, 63 (1988).
5. M.B. Tsang et al., Phys. Lett. B220, 492 (1989).
6. J.Péter et al., Nucl. Phys. A519, 611 (1990).
7. W.J. Llope et al., Phys. Rev. C51, 1325 (1995).
8. L. Phair et al., Nucl. Phys. A548 (1992) 489.
9. L. Phair et al., Nucl. Phys. A564 (1993) 453.
10. D.X. Jiang et al., Nucl. Phys. A503, 560 (1989).
11. R.T. de Souza et al., Phys. Lett. B268, 6 (1991).
12. B. Lott et al., Phys. Rev. Lett. 68, 3141 (1992).
13. J. Tõke et al., Phys. Rev. Lett. 75, 2920 (1995).
14. M. D'Agostino et al., Phys. Lett. B371, 175 (1996).
15. M. D'Agostino et al., Phys. Lett. B371, 175 (1996).
16. G.J. Kunde et al., Phys. Rev. Lett. 77, 2897 (1996).
17. W.U. Schröder, University of Rochester Report DOE/ER/7904' unpublished.
18. R.T. de Souza et al., Nucl. Instr. and Meth. A295, 109 (1990).
19. M.B. Tsang et al., Phys. Rev. Lett. 71, 1502 (1993).
20. C.B. Chitwood et al., Phys. Rev. C34, 858 (1986).
21. M.B. Tsang et al., Phys. Rev. C44, 2065 (1991).
22. L. Phair et al., Phys. Rev. Lett. 77, 822 (1996).
23. R. Lacey et al., Phys. Rev. Lett. 70, 1224 (1993).
24. Phys. Rev. C44, 2865 (1991).
25. R. Popescu et al., Phys. Rev. C54, 796 (1996).

MULTI-FRAGMENT PRODUCTION FOR REACTIONS OF $^{112}Sn + ^{112}Sn$ and $^{124}Sn + ^{124}Sn$ at E/A = 40 MeV

G.J. Kunde, S.J. Gaff, C.K. Gelbke, T. Glasmacher, M.J. Huang, R. Lemmon, W.G. Lynch, L. Manduci, L. Martin, M.B. Tsang, W.A. Friedman[a], J. Dempsey[b], R.J. Charity[b], L.G. Sobotka[b], D.K. Agnihotri[c], B. Djerroud[c], W.U. Schröder[c], W. Skulski[c], J. Tõke[c], and K. Wyrozebski[c]

Hot nuclear systems formed in intermediate energy nucleus-nucleus collisions are known [1-8] to decay by copious production of intermediate mass fragments (IMF's) characterized by $3 \leq Z_{IMF} \leq 20$. In examining reactions of Xe on various targets covering a wide range of masses, a near-universal correlation has previously been observed between the average number of emitted IMFs, $< N_{IMF} >$, and the charged particle multiplicity, NC [7]. In reactions, using reversed kinematics, with Au beams on a variety of targets, a similar universal correlation (independent of target mass) was also observed between $< N_{IMF} >$ and the total charge contained in fragments having two or more charges, which were observed near the projectile rapidity [8-10]. The universality seen in these instances was interpreted as due to a decay mechanism, independent of the production of the decaying system.

Only a few studies have addressed the influence of the neutron number of the projectile or target. Observables studied so far were isotopic yields of fragments [11-13] and isobaric ratios [14]. In this letter we investigate the influence of the neutron number in the target and projectile on the correlation of $< N_{IMF} >$ with the multiplicities of the yields of different types of particles: charged particles (N_C), neutrons (N_N), and light-charged particles with $Z \leq 2$ (N_{LC}) [15]. The measurement involves reactions with two projectile-target combinations of fixed proton number (to keep the influence of the Coulomb force constant), but very different neutron numbers.

Two symmetric reactions, $^{112}Sn + ^{112}Sn$ and $^{124}Sn + ^{124}Sn$, were studied at a beam energy of E/A = 40 MeV. The beams were accelerated by the K1200 cyclotron and used to bombard targets of approximately $5 mg/cm^2$ areal density.

For each event, the associated neutron multiplicity was measured with the SuperBall neutron multiplicity meter [18] and charged particles were detected in 280 plastic scintillator - CsI(Tl) phoswich detectors of the Miniball/Miniwall array [19]. The charged particle arrays provided isotopic resolution for H and He nuclei and elemental resolution for heavier fragments with approximate energy thresholds of $E_{th}/A \approx 2.2$ MeV (4.5 MeV) for Z=3 (Z=10) particles detected in the Miniwall at $5.4° \leq \Theta_{lab} \leq 25°$ and $E_{th}/A \approx 1.5$ MeV (2.5 MeV) for Z=3 (Z=10) particles detected in the Miniball at $25° \leq \Theta_{lab} \leq 160°$ respectively.

Figure 1 shows the observed average neutron multiplicities, $< N_N >$, as a function of charged-particle multiplicity, N_C. Since heavy nuclei of moderate excitation energy decay primarily by neutron emission, the event trigger largely suppresses very peripheral collisions characterized by low neutron multiplicities. For a given value of N_C, larger neutron multiplicities are observed for $^{124}Sn + ^{124}Sn$ than for $^{112}Sn + ^{112}Sn$.

Figure 2 shows the average number of detected intermediate mass fragments ($< N_{IMF} >$: $Z \geq 3$) as a function of N_C (points, left panel), N_{LC} (curves, left panel), and N_N (points, right panel) for the two reactions studied. Distinct differences are observed which are incompatible with a universal scaling of $< N_{IMF} >$ with N_C, N_{LC}, or N_N. Relative to the respective curves for $^{112}Sn + ^{112}Sn$, the $< N_{IMF} >$ versus N_C and N_{LC} curves for $^{124}Sn + ^{124}Sn$ are shifted to lower values of N_C and N_{LC}, while the $< N_{IMF} >$ versus N_N curve is shifted to higher values of N_N. At any given value of N_C or N_{LC}, $< N_{IMF} >$ is larger for

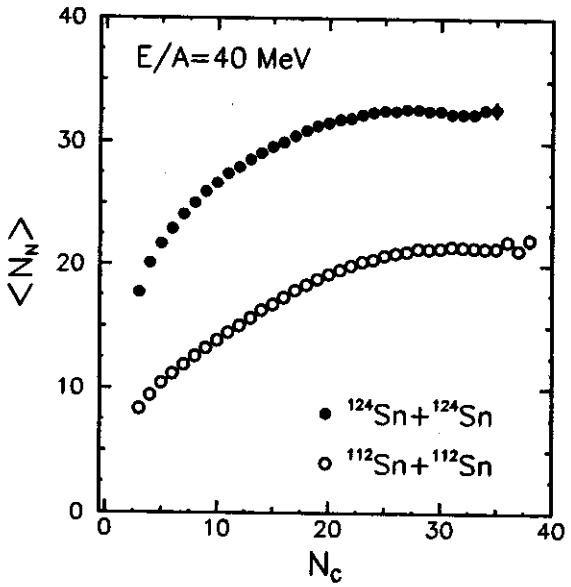

Figure 1: Average neutron multiplicities, $< N_N >$, as a function of charged-particle multiplicity, N_C, for ^{112}Sn + ^{112}Sn and ^{124}Sn + ^{124}Sn collisions at E/A = 40 MeV.

^{124}Sn + ^{124}Sn than for ^{112}Sn + ^{112}Sn. The same is true for very high values of N_N, where the $< N_{IMF} >$ versus N_N curves have leveled off, but in the region where $< N_{IMF} >$ grows monotonically with increasing N_N, the fragment multiplicity at a given value of N_N is larger for ^{112}Sn + ^{112}Sn than for ^{124}Sn + ^{124}Sn collisions. Roughly consistent with the larger mass of the ^{124}Sn + ^{124}Sn system, the maximum values of $< N_{IMF} >$ are about 10% larger for ^{124}Sn + ^{124}Sn than for ^{112}Sn + ^{112}Sn. Rather surprisingly, the maximum $< N_{IMF} >$-values extracted as a function of N_C are about 50% larger than those extracted as a function of N_N; those extracted as a function of N_{LC} lie in between.

The qualitative trends observed in Fig. 2 are predicted by statistical calculations and are thus largely driven by phase space. To demonstrate this, we use the expanding evaporating source (EES) model of ref. [16] which has been successful in explaining a number of features observed in multifragment emission processes [5,6,16,17]. Since correlations between $< N_{IMF} >$ and N_C depend only weakly on the total mass of the assumed source [5,7], we restrict our schematic calculations to the idealized case of a source made up of the total mass and charge of projectile and target (labeled as $^{224}_{100}$X and $^{248}_{100}$X). Thus, our calculations are best suited for collisions where the overlap of projectile and target is large. For simplicity, we assumed a flat distribution of initial temperatures covering an interval of excitation energies per nucleon of 1.3 MeV $\leq E^*/A \leq$ 10 MeV (maximal available energy in the cm-system)

Figure 3 shows multiplicity correlations calculated for ^{112}Sn + ^{112}Sn and ^{124}Sn + ^{124}Sn. Both the direction and the relative magnitude of the shift between the various multiplicity correlations noted in Fig. 2 are approximately reproduced. The calculations also reproduce the qualitative differences between the maximum values of $< N_{IMF} >$ observed at large N_C, N_{LC}, and N_N.

To illustrate similarities and differences predicted by the model for the decay of the two systems, we show in Fig. 4 the predicted time-dependence of source temperatures (dotted curves, right hand scale) and emission rates of neutrons, light charged particles, and IMFs (dashed, solid, and dot-dashed curves, respectively, left hand scale) assuming a single initial excitation energy per nucleon of E^*/A = 10 MeV. Initially, the two sources cool by expansion and light particle emission with very minor differences in their cooling rates. When the sources reach their minimum density (at T $\approx$ 5-6 MeV), they are predicted to decay

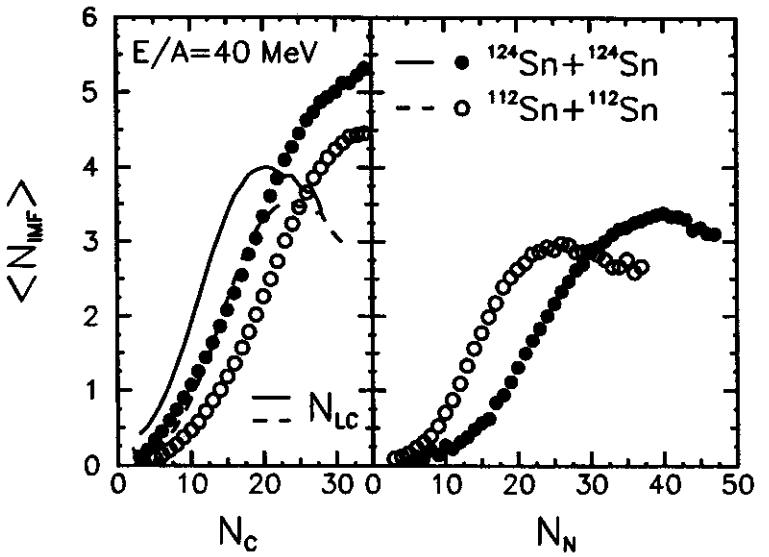

Figure 2: Average fragment multiplicities, $< N_{IMF} >$, as a function of charged-particle and light-charged-particle multiplicities (N_C and N_{LC}, left panel) and neutron multiplicities (N_N, right panel) for ^{112}Sn + ^{112}Sn (open points and dashed curves) and ^{124}Sn + ^{124}Sn (solid points and solid curves) collisions at E/A = 40 MeV.

by copious IMF production. In the model, the system resides for a relatively long time (≈ 100 fm/c) in this low-temperature, low-density configuration (note the logarithmic time scale), and nearly all fragments are emitted during this time interval. After this stage the model sources have lost approximately 1/3 of their original mass and their N/Z ratios have changed from 1.48 (1.24) to approximately 1.45 (1.30) for the neutron rich (neutron poor) systems. A modest subsequent rise in temperature is predicted when the sources contract back to near-normal nuclear density, but subsequent particle emission is less important. The model predicts very different neutron and light-charged-particle emission rates for the two systems, but similar IMF production rates.

Figure 5 shows model predictions of the average initial excitation energy per nucleon, $< E^*/A >$, selected by sharp cuts on N_C, N_{LC} or N_N. Over a significant range of multiplicities, $< E^*/A >$ is proportional to N_C, N_{LC} and N_N. (The flat regions at low and high multiplicities are associated with the sharp edges of the assumed flat initial temperature distribution.) A cut on N_C or N_{LC} selects a higher value of $< E^*/A >$ (and thus a higher value of $< N_{IMF} >$) for the neutron-rich system, but a cut on N_N selects a lower value. The relative difference in excitation energy selection is more pronounced for cuts on N_N than for cuts on N_C or N_{LC}. The offset between the $< N_{IMF} >$ versus N_C, N_{LC} or N_N curves in Fig. 2 can thus be understood as due to the fact that specific cuts on N_C, N_{LC} or N_N select different initial conditions for the two systems.

Maximum $< N_{IMF} >$ values extracted from $< N_{IMF} >$ versus N_C, N_{LC} and N_N correlations are surprisingly different, see Fig. 2. Within the EES model, these difference arise from two effects. First, the intrinsic resolution of neutron and charged particle multiplicity filters is different. For example, sharp cuts in N_C, N_{LC} and N_N, chosen to select the same average excitation energy per nucleon, $< E^*/A >$ = 7 MeV, for the $^{224}_{100}$X ($^{248}_{100}$X) system, filter out E^*/A - distributions of variances $\sigma^2(E^*/A) \approx$ 0.9, 1.32, and 1.82 MeV^2 (0.9, 1.36, 1.64 MeV^2), respectively; i.e., the resolution is predicted to be best for cuts on N_C. Second, in the extreme tails of the N_C, N_{LC}, and N_N distributions, auto-correlations due to energy conservation become apparent. If, for example, all reactions had a single initial excitation energy, the selection of very high neutron or light-charged-particle multiplicity events would produce a sample of

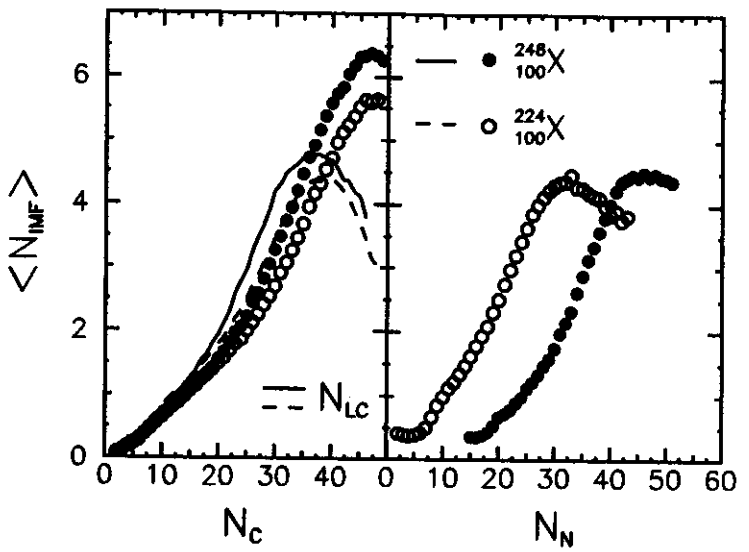

Figure 3: Average fragment multiplicities, $< N_{IMF} >$, predicted by the EES model as a function of charged-particle and light-charged-particle multiplicities (N_C and N_{LC}, left panel) and neutron multiplicities (N_N, right panel) for ^{112}Sn + ^{112}Sn and ^{124}Sn + ^{124}Sn. Details of the calculations are discussed in the text.

reduced IMF multiplicity, i.e. N_N and N_{IMF} (and also N_{LC} and N_{IMF}) are anti-correlated. The opposite is true for N_C and N_{IMF}, because IMFs are included in the definition of N_C [15]. These auto-correlations arise in our model calculations – which predict that they become significant in the extreme tails of the multiplicity distributions. For example, calculations at a fixed initial excitation energy per nucleon of E^*/A = 9 MeV predict a change of $\Delta < N_{IMF} > \approx +1(-1)$ when the selecting gate on N_C (N_N) is increased by ΔN_C (ΔN_N) $\approx$ 10 from its average value.

The effects of these auto-correlations can be studied in the calculations by comparing the average yields calculated at a fixed temperature with the yields which reflect event-to-event fluctuations. As an example we consider calculations for $^{224}_{100}$X. For the highest initial excitation energy used in determining the yields, E^*/A = 10 MeV, the average predicted multiplicities are: $\overline{N_{IMF}}$ = 5.2, $\overline{N_C}$ = 41.5, $\overline{N_{LC}}$ = 36.2, and $\overline{N_N}$ = 28.9 [21]. The point ($\overline{N_C}$, $\overline{N_{IMF}}$) lies close to the calculated $< N_{IMF} >$ versus N_C curve in Fig. 3, but values of $< N_{IMF} >$ larger than $\overline{N_{IMF}}$ are obtained for $N_C > \overline{N_C}$ due to the positive correlation between N_{IMF} and N_C explained above. In contrast, the maxima of the $< N_{IMF} >$ versus N_{LC} (N_N) curves are smaller than $\overline{N_{IMF}}$, and there are clear signs of an anti-correlation between N_{IMF} and N_{LC} (N_N) in Fig. 3 when N_{LC} (N_N) is significantly larger than $\overline{N_{LC}}$ ($\overline{N_N}$).

The relative magnitudes of resolution and auto-correlation effects in the tails of the multiplicity distributions depend on the assumed distribution of initial excitation energies and on contributions of prompt particles, and can thus not be disentangled in a model-independent way.

In summary, large differences in the correlations of average IMF multiplicities with neutron, charged-particle, and light-charged-particle multiplicities were observed for ^{112}Sn + ^{112}Sn and ^{124}Sn + ^{124}Sn reactions. These differences can be understood by statistical calculations for an ensemble of expanding evaporating sources representing a broad range of initial temperatures. In the calculations, the observed effects are due to different cooling rates from neutron and light-charged-particle emission, differences in resolution of reaction filters based upon neutron and charged particle multiplicity measurements, and auto-correlations between various emission types at high multiplicities.

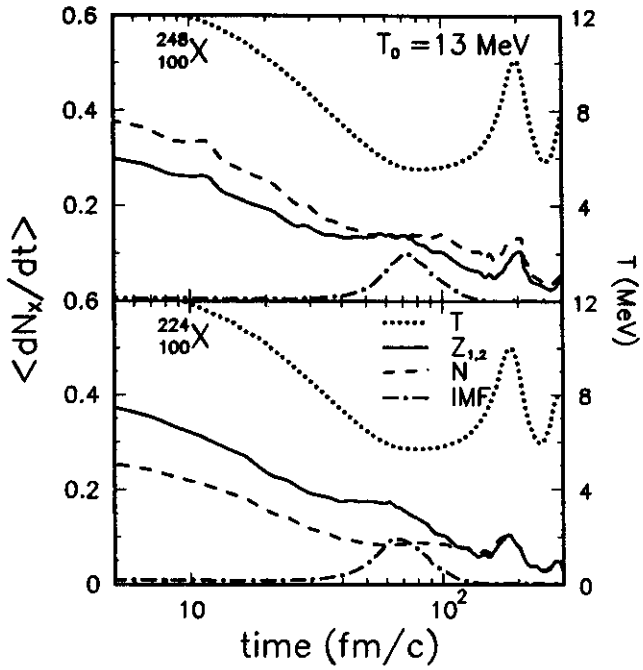

Figure 4: Particle emission rates and cooling curves predicted by the EES model for initial source temperatures of 13 MeV. Top and bottom panels show results for ^{112}Sn + ^{112}Sn and ^{124}Sn + ^{124}Sn, respectively.

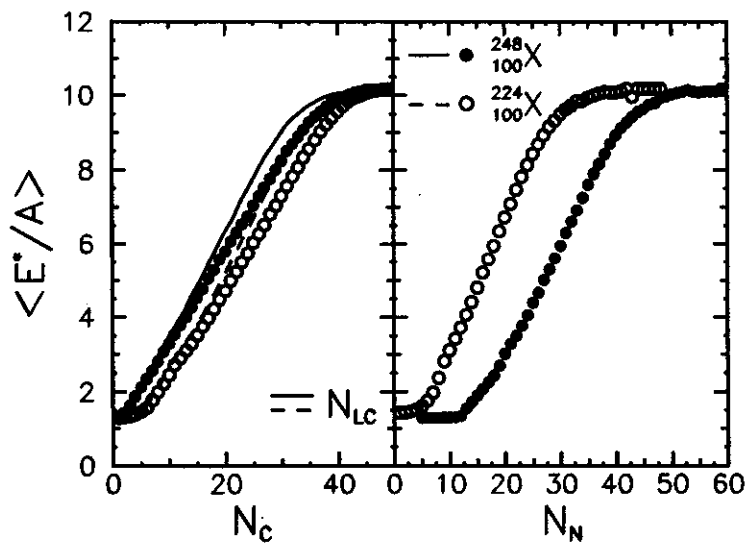

Figure 5: Average source excitation energy per nucleon, $< E^*/A >$, selected by sharp cuts on N_C and N_{LC} (circles points and lines, left panel) and N_N (points, right panel) as predicted by EES calculations for ^{112}Sn + ^{112}Sn and ^{124}Sn + ^{124}Sn.

a.Department of Physics, University of Wisconsin, Madison, WI 53706, USA
b.Department of Chemistry, Washington University, St. Louis, MO 63130, USA
c.Department of Chemistry and Nuclear Structure Research Laboratory, University of Rochester, Rochester, NY 14627, USA

References

1. D.H.E. Gross, Rep. Progr. Phys. 53, 605(1990).
2. L. G. Moretto and G. J. Wozniak, Ann. Rev. Nucl. Part. Sci. 43, 379 (1993) and references quoted therein.
3. J.P. Bondorf, A.S. Botvina, A.S. Iljinov, I.N. Mishustin and K. Sneppen, Phys. Rep. 257, 133 (1995).
4. C.A. Ogilvie et al., Phys. Rev. Lett. 67, 1214 (1991).
5. D.R. Bowman et al., Phys. Rev. Lett. 67, 1527 (1991).
6. R.T. de Souza et al., Phys. Lett. B268, 6 (1991).
7. D.R. Bowman et al., Phys. Rev. C46, 1834 (1992).
8. P. Kreutz et al., Nucl. Phys. A556, 672 (1993).
9. J. Pochodzalla et al., Nucl. Phys. A583, 553c (1995).
10. W. Trautmann et al., to be published.
11. J. Brzychczyk et al., Phys. Rev. C47, 1553 (1993).
12. S.J. Yennello et al., Phys. Lett. 321B, 15 (1994).
13. R. Wada et al., Phys. Rev. Lett. 58, 1829 (1987).
14. Yu. Murin et al., Phys. Rev. C51, 2794 (1995).
15. In our definition, $N_C = N_{LC} + N_{IMF} + N_{NID}$, where N_{LC}, N_{IMF}, and N_{NID} denote the multiplicities of light-charged-particles, of intermediate mass fragments, and of non-identified charged particles with $Z \geq 3$, respectively.
16. W.A. Friedman, Phys. Rev. Lett. 60 (1988) 2125; and Phys. Rev. C42 (1990) 667.
17. C. Schwarz et al., Phys. Rev. C48, 676 (1993) and refs. given therein.
18. W.U. Schröder, University of Rochester Report DOE/ER/79048-1, 1995, unpublished.
19. R.T. de Souza et al., Nucl. Instr. and Meth. A295, 109 (1990); M.B. Tsang et al., Phys. Rev. Lett. 71 (1993) 1502.
20. C.P. Montoya et al., Phys. Rev. Lett. 73, 3070 (1994).
21. We use a different notation for the average values at fixed $E^*/A = 10$ MeV to distinguish them from the average IMF multiplicities, $< N_{IMF} >$, extracted from cuts on the fluctuating quantities N_C, N_{LC}, or N_N.

SIGN DEPENDENCE OF SPIN POLARIZATION OF FRAGMENTS PRODUCED FOLLOWING INTERMEDIATE-ENERGY PROJECTILE FRAGMENTATION

P.F. Mantica, R.W. Ibbotson, D. W. Anthony, M. Fauerbach, D.J. Morrissey, C.F. Powell, J. Rikovska,[a,b] M. Steiner, N.J. Stone,[a] and W.B. Walters[b]

Large spin polarization of secondary fragments produced at small angles to the central beam axis by intermediate-energy, heavy-ion reactions was observed by Asahi *et al.* [1]. For ^{12}B fragments produced in the reaction of a 40.6 MeV/nucleon ^{14}N beam on an Au target at an incident beam angle of 5°, sizable polarization (up to 20%) was detected over the whole range of the ^{12}B momentum distribution except at the peak of the momentum yield curve where the polarization was measured to be zero. Dependence of the spin polarization on the residual momentum of the observed fragment was explained using a general kinematical model of projectile fragmentation [1], assuming straight-line trajectories and same-side scattering of the residual fragment away from the target. Assuming that the nucleons removed in the fragmentation process are from a localized position within the projectile, coupling the radius vector R describing this position in the projectile rest frame with the momentum vector of the removed nucleons, $\mathbf{k_r}$, will constitute the angular momentum of the residual fragment. This resultant angular momentum is dependent on the residual fragment momentum $\mathbf{p_f}$ through the relation $\mathbf{p_f} = m\mathbf{v_0} - \mathbf{k_r}$, where m and $\mathbf{v_0}$ are the residual fragment mass and the projectile velocity, respectively. Residual fragments having momenta greater than $m\mathbf{v_0}$ will have a preferred orientation of the angular momentum which is of opposite sign to fragments having momenta less than $m\mathbf{v_0}$. In addition, residual fragments with momenta equal to $m\mathbf{v_0}$ are expected to show no polarization.

The systematic behavior of the spin polarization following projectile fragmentation reactions was measured for different targets and incident beam energies [2]. There was a clear dependence of the spin polarization on both the atomic number of the target and the primary beam energy. In general, it was found that the simple kinematical picture of Asahi *et al.* [1] could predict the gross behavior of the spin polarization of fragments produced in intermediate-energy reactions for light-A projectiles. Some of the observed polarization curves, however, revealed non-zero values for the fragment spin polarization at the peak in the momentum yield curve (where $\mathbf{p} = m\mathbf{v_0}$). This has been attributed to nucleon rescattering in the residual fragment [2]. This result is significant as secondary fragments could then be produced with large spin polarization at the peak in the production curve, giving assistance to the study of ground state moments of exotic nuclei (see, for example, Ref. [3]).

An additional prediction of the simple kinematical picture of spin polarization produced in projectile fragmentation reactions is that a change in the incident beam angle on target from positive to negative should result in a change in sign of the residual fragment polarization. This point could not be verified in the earlier measurements at RIKEN due to technical limitations on the beam steering dipole magnets located upstream of the RIPS spectrometer target position [4]. We have measured the spin polarization as a function of both the incident beam angle (positive and negative) on target and the secondary fragment momenta for ^{12}B fragments produced in the reaction of an ^{18}O primary beam at 80 MeV/nucleon on a 214 mg/cm^2 Nb target at the NSCL. Here the A1200 fragment separator was used to select the desired fragments. Since the A1200 is a zero-degree spectrometer, two dipole magnets located between the exit of the K1200 Cyclotron and the A1200 target box were used to steer the primary beam onto the production

target, allowing for the collection of fragments in the range $-3°$ to $+3°$. The horizontal acceptance of the A1200 for the target position in the present experiment was $\approx 1°$, while the momentum acceptance was set to 1% of the central $B\rho$ with a slit at the first momentum-dispersed image of the spectrometer. A 425 mg/cm^2 Al degrader wedge with a slope angle of 3.5 mrad was placed at the second dispersive image of the A1200 to separate fragment isotopes with a given mass-to-charge ratio based on A and Z. Identification of ^{12}B secondary fragments was accomplished at both the A1200 focal plane and the experimental endstation using the energy loss of the fragments measured in 300 μm Si PIN detectors and the fragment time-of-flight (TOF) relative to the K1200 Cyclotron radiofrequency.

The polarization measurements were made using the technique of nuclear magnetic resonance of β-emitting nuclei (β-NMR). A β-NMR endstation has been developed at the NSCL and is described in Ref. [5]. The ^{12}B ($T_{1/2}$ = 20 ms) polarization measurements required pulsing of the K1200 Cyclotron beam. Pulse timing was controlled by the data acquisition computer, and parameters were selected to allow for a 20 ms fragment implantation (beam-on) time and a data collection (beam-off) time was 40 ms. During beam-on cycles, ^{12}B fragments were energy degraded to $\approx$ 13 MeV/nucleon using Al foils, collimated, and implanted into the Pt catcher foil, which was annealed for 10 h at 630° C in air. β particles which produced signals above threshold in both elements of either β telescope were recorded in the event stream during the beam-off cycles only. On alternating beam-off cycles, a frequency-modulated (FM) RF signal was introduced to the implanted sample for the duration of the beam-off period. The applied RF signal for all data points was set to the resonance peak for ^{12}B , with a frequency modulation of $\pm$ 30 kHz. The ratio of the counting rates in the 0° (Up) and 180° (Down) β telescopes incorporated in the β-NMR system for both RF-on and RF-off conditions

$$R = \frac{(\mathrm{Up/Down})_{\mathrm{RF-on}}}{(\mathrm{Up/Down})_{\mathrm{RF-off}}} \tag{1}$$

is the observed NMR effect, and is related to the magnitude of the fragment polarization.

We measured the spin polarization of the ^{12}B fragments as a function of the longitudinal fragment momenta. Our results are shown in Figure 1 where the NMR effect is plotted versus the deviation of the ^{12}B fragment momenta from the peak of the momentum yield curve. For the ^{12}B fragments collected at +3° relative to the primary beam axis, one observes that there is polarization of the ^{12}B fragments at the value $\Delta p/p$ = 0%. This confirms the result of Okuno *et al.* [2] that intermediate mass targets produce non-zero values for the polarization at the peak in the momentum yield curve. The polarization of the ^{12}B fragments collected at a beam angle of +3° shows little dependence on the fragment momentum in the range -2% $\leq \Delta p/p \leq$ +2%. This also corroborates the results reported in Ref. [2], where only a small dependence of the ^{13}B polarization was observed over the same range of fragment momenta for the reaction of ^{15}N on ^{93}Nb at 67.3 MeV/nucleon.

The dependence of the ^{12}B polarization on the incident beam angle is also shown in Figure 1. We observed a change in the sign of the polarization of ^{12}B fragments with a change in the direction of the incident angle of the primary ^{18}O beam from +3° to -2.5°. This result supports the hypothesis in Ref. [1] that the mean deflection angle for the projectile-like fragments, and hence the dominance of near- or far-side trajectories, determines the sign of the observed spin polarization. For ^{12}B fragments collected at 0° relative to the normal beam axis, no polarization was observed. These results are in agreement with the preliminary results obtained for the production of spin-polarized ^{37}K fragments following high-energy

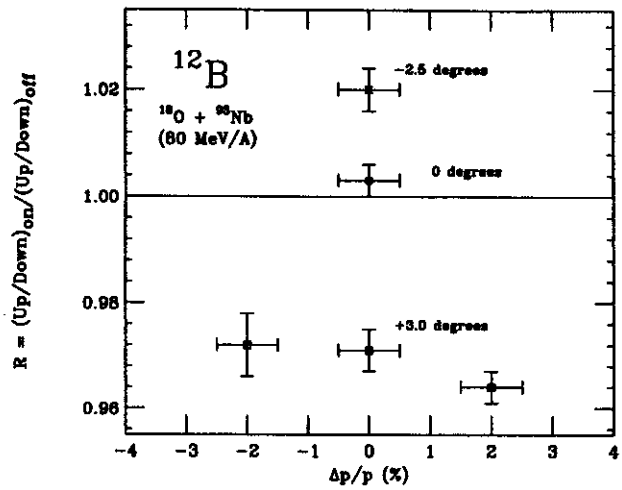

Figure 1: Dependence of the spin polarization on the momenta of ^{12}B fragments. Measurements were made for positive deflection (□), negative deflection(×), and normal incidence (○) of the primary ^{18}O beam on the Nb target at 80 MeV/nucleon. The values $\Delta p/p$ give the deviation of the momentum of ^{12}B fragments from the peak of the momentum yield curve. The error bars on these values indicate the momentum acceptance of the A1200.

(500 MeV/nucleon) fragmentation [6] at GSI.

a. Department of Physics, Oxford University, Oxford OX1 3PU, United Kingdom.
b. Department of Chemistry and Biochemistry, University of Maryland, College Park, MD 20742.

References

1. K. Asahi *et al.*, Phys. Lett. B251, 488 (1990).
2. H. Okuno *et al.*, Phys. Lett. B335, 29 (1994).
3. H. Ueno *et al*, Phys. Rev. C53, 2142 (1996).
4. T. Kubo *et al.*, Nucl. Instr. Methods B70, 309 (1992).
5. P.F. Mantica *et al.*, this Annual Report and Phys. Rev. C56, 2501 (1997).
6. W.-D. Schmidt-Ott *et al.*, *Nachrichten*, GSI Report 12-95, pp. 8-9, 1995.

PRODUCTION OF HEAVY Ni ISOTOPES FOLLOWING ^{86}Kr FRAGMENTATION

P.F. Mantica, R.W. Ibbotson, D.W. Anthony, M. Fauerbach, R. Harkewicz, D.J. Morrissey, C.F. Powell, and D. Seweryniak[a,b]

The single-particle level ordering in nuclei far from the line of β stability is fundamental in the formulation of theoretical models used to describe interactions and predict new physics phenomena in exotic nuclear systems. For the neutron-rich isotopes along the $Z = 28$ closed shell, the experimental determination of single-proton and single-neutron states in the odd-mass Cu and Ni isotopes, respectively, can provide a more accurate basis for the understanding of extremely neutron-rich nuclei in the region of doubly-magic $^{78}_{28}Ni_{50}$. The low energy structure and decay properties of these neutron-rich Cu and Ni nuclei are also important in the development of astrophysical r-process calculations and in understanding the $A \sim 80$ solar abundance puzzle [1].

Steady advances have been made in the study of the decay of the neutron-rich Ni isotopes in recent years, attributed mainly to developments at projectile fragmentation facilities. The doubly closed-shell nucleus ^{78}Ni has been identified [2] following the relativistic fission of ^{235}U at GSI. β-decay half-lives have been determined [3] for the heavy Ni isotopes up to ^{76}Ni. However, only limited experimental data are available for excited levels in the neutron-rich Ni and the neighboring odd-proton Cu nuclides.

We have completed a measurement of the production rates of the neutron-rich Ni isotopes produced following fragmentation of an 80 MeV/nucleon ^{86}Kr beam on a Be target. Our interest was the measurement of production cross sections for heavy Ni isotopes to determine the feasibility of completing decay spectroscopy ($\beta\gamma$ and βn) experiments towards ^{78}Ni. Weber *et al.* [4,5] deduced experiment production cross sections for the heavy $_{21}$Sc through $_{28}$Ni isotopes following fragmentation of an ^{86}Kr beam at 500 MeV/nucleon on targets of Be, Cu, and Ta, and their results agreed within an order of magnitude with the various models (semi-empirical parameterization, geometrical abrasion model, and internuclear cascade) for projectile fragmentation. The semi-empirical parameterization EPAX [6], however, tended to overpredict the production cross sections for very proton-rich and neutron-rich isotopes. Pfaff *et al.* studied in detail the fragmentation of an ^{86}Kr beam at 70 MeV/nucleon with an ^{27}Al target at the NSCL, and found similar agreement with the ISAPACE model [7] and EPAX parameterization for nuclei produced from As ($Z = 33$) through Y ($Z = 39$).

For the experiments reported here, an $^{86}Kr^{23+}$ beam was extracted from the superconducting ECR source and accelerated to 80 MeV/nucleon using the K1200 Cyclotron. The typical beam intensity of ^{86}Kr measured immediately before the A1200 target position was 0.7 particle nA. The beam was then incident on a 160 mg/cm^2 Be target at the entrance to the A1200 fragment separator. The momentum acceptance of the A1200 was set to 0.25% using a slit at the first dispersive image. Fragment identification was accomplished at the A1200 focal plane using the energy-loss detected in a 300 μm Si PIN detector and the fragment time-of-flight measured between a total energy plastic scintillator detector at the focal plane and the K1200 Cyclotron radio-frequency.

A typical energy loss versus time of flight diagram for a central $B\rho$ setting of 2.996 Tm, which corresponds to the peak in production of ^{71}Ni, is shown in Figure 1. Our study focussed on the production of ^{70,71,72}Ni, and therefore we limited our measurements to a range in $B\rho$ from 2.99 to 3.07 Tm. Experimental production rates were determined by considering the total fragment collection time, the primary beam

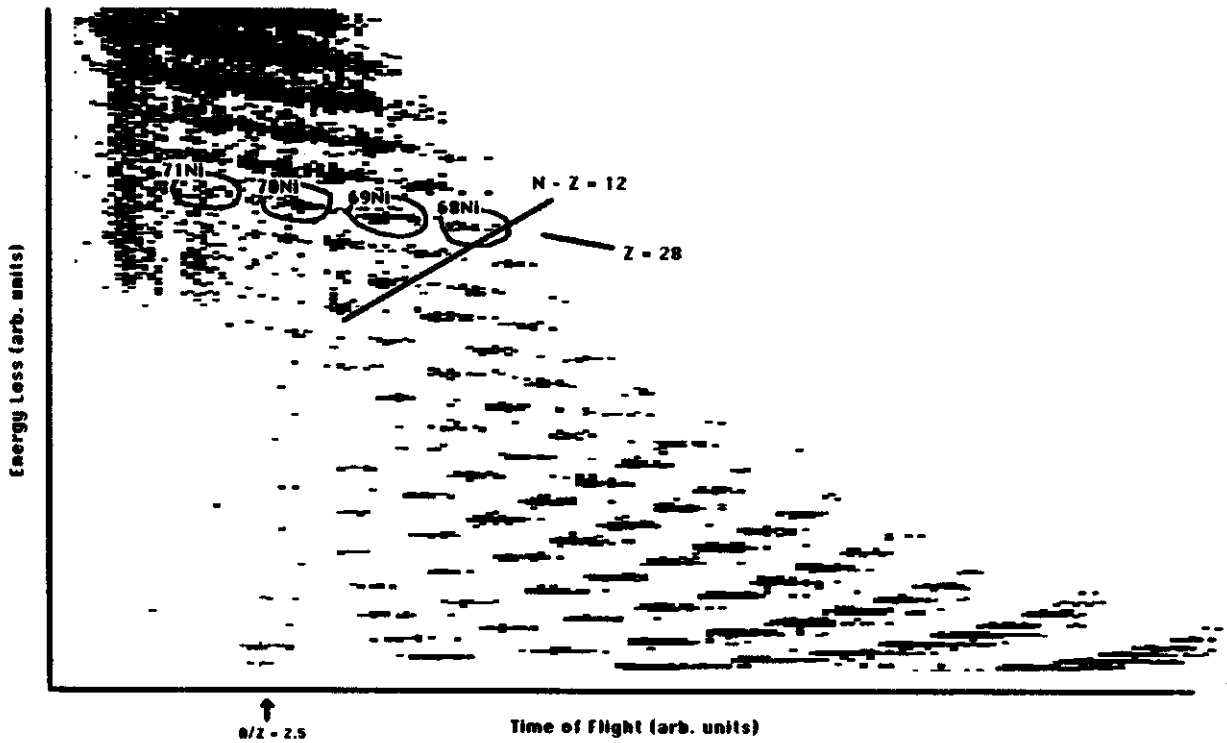

Figure 1: Energy loss versus time of flight diagram for fragments produced in the reaction of ^{86}Kr + ^{9}Be at 80 MeV/nucleon. The A1200 magnet settings are set to the peak in the production cross section for ^{71}Ni.

intensity on target, and the data acquisition dead time. The measured production rates for ^{68,70,72}Ni in fragments/sec for 1 particle nA of ^{86}Kr primary beam are shown in Figure 2. Also included in Figure 2 are the production rates for these isotopes extracted from the code INTENSITY [8], which estimates secondary beam intensities from a projectile fragmentation separator based on cross sections calculated using the EPAX parameterization. The observed Ni isotopes have experimental production rates which are a factor of 5 below that predicted by INTENSITY, reaffirming the fact that the EPAX parameterization overpredicts the production rates of neutron-rich nuclei.

The production rate of $\approx$ 4 min^{-1} for ^{72}Ni is not sufficient to attempt β delayed γ spectroscopy experiments. Our goal at present is to look at the development of primary beams of ^{76}Ge and ^{82}Se to improve the production rates of heavy Ni isotopes at the NSCL. The estimated production rate from INTENSITY, for example, for ^{71}Ni using a primary beam of ^{76}Ge at 70 MeV/A on a 170 mg/cm^2 Be target is 30 fragments/sec for 1 particle nA of primary beam. Taking into account the overproduction factor, this is a factor of 30 increase in the production rate over the ^{86}Kr, which may allow $\beta\gamma$ and βn studies of this isotope.

a. Physics Division, Argonne National Laboratory, Argonne, IL 60439.
b. Department of Chemistry and Biochemistry, University of Maryland, College Park, MD 20742.

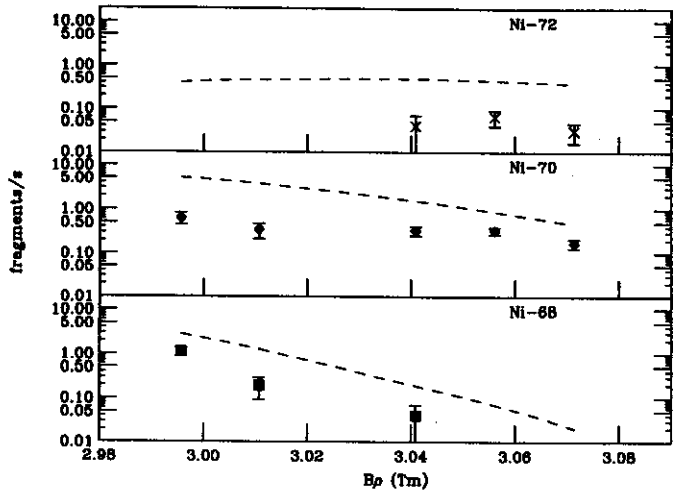

Figure 2: Production rates for ^{68,70,72}Ni following fragmentation of a 80 MeV/nucleon ^{86}Kr beam on a ^{9}Be target. The dashed lines are the predicted intensities from INTENSITY [8].

References

1. K.-L. Kratz *et al.*, Z. Phys. A332, 419 (1989).
2. Ch. Engelmann *et al.*, Z. Phys. A352, 351 (1995).
3. F. Amiel, *GSI Nachrichten* 11-95, 19 (1995).
4. M. Weber *et al.*, Z. Phys. A343, 67 (1992).
5. M. Weber *et al.*, Nucl. Phys. A578, 659 (1994).
6. K. Sümmerer *et al.*, Phys. Rev. C42, 2546 (1990).
7. M. Fauerbach, Diploma thesis, TH Darmstadt, 1992.
8. J.A. Winger, B.M. Sherrill, and D.J. Morrissey, Nucl. Instrum. Methods Phys. Res. B70, 380 (1992).